Ore Geology Reviews 72 (2016) 485–509

Contents lists available at ScienceDirect

Ore Geology Reviews

journal homepage: www.elsevier.com/locate/oregeorev

Mineral exploration and basement mapping in areas of deep transported cover using indicator heavy minerals and paleoredox fronts, Yilgarn Craton, Western Australia

Walid Salama [a,b,c,*], Ravi R. Anand [a,b], Michael Verrall [a]

[a] CSIRO, Mineral Resources Flagship, 26 Dick Perry Avenue, Kensington WA 6151, Perth, Australia
[b] Deep Exploration Technologies CRC, The University of Adelaide, Adelaide, SA 5005, Australia
[c] Department of Geology, Faculty of Science, Cairo University, Giza, Egypt

ARTICLE INFO

Article history:
Received 1 January 2015
Received in revised form 15 July 2015
Accepted 21 July 2015
Available online 23 July 2015

Keywords:
Diamictites
Indicator minerals
Geochemistry
Yilgarn Craton
Western Australia

ABSTRACT

Glacial sediments have been thoroughly integrated into mineral exploration protocols in the Northern hemisphere (e.g., Canada and Fennoscandia), but have received less attention in Australia. In Western Australia (WA), Permo-Carboniferous diamictites, buried by younger Cenozoic sediments, cover scattered areas that have potential to host gold and nickel mineralization, in the NE of the Yilgarn Craton. A systematic stratigraphic, mineralogical and geochemical study was undertaken to determine whether diamictites in the Agnew–Lawlers gold province have properties that may help target concealed mineralization. At the Agnew–Lawlers District, rocks intersected in 31 drill holes NE of the Waroonga gold mine, were interpreted in terms of lithological, textural and paleolandscape, mineralogical and geochemical variations to select the best sampling media for mineral exploration and provenance assessment. The paleotopographic variation, asymmetry of the depositional basin, polymictic composition, matrix-supported, mixed angular and rounded and poorly sorted texture of the diamictite clasts indicate mechanical dispersal from proximal and distal, heterogeneous source rocks. Ferromagnesian minerals, chromite, Cr-magnetite, magnetite and Ni–Cu–Fe sulfides are abundant in the diamictite close to mafic–ultramafic source rocks. Monazite, apatite, zircon and clasts derived from pyrite-bearing quartz veins increase in abundance in the diamictite close to the Waroonga shear zone that separates granitoid/gneiss terrain from the Scotty Creek metasediments. Ilmenite is extensively distributed in diamictites throughout the study area and its Mn content can be used to differentiate between felsic and mafic source rocks. Alteration of ilmenite to titanite, monazite to apatite and thorite, and replacement and fracture-filling of pentlandite to monazite suggest felsic, intrusive-related hydrothermal alteration of the source rocks prior to mechanical weathering. Late Paleozoic tropical weathering associated with oscillation of water table and icehouse to greenhouse climatic shift has created paleoredox fronts in the Permo-Carboniferous sequence. Below the redox fronts, diamictites are unweathered, rich in detrital sulfide and opaque oxide minerals and can be used in provenance studies and tracing mineralization. These characteristics of unweathered diamictite are the optimal sampling medium target for provenance studies and mineral exploration. These are cemented mainly by calcareous cement where they overlie mafic–ultramafic rocks and by pyrite cement where they overlie the Scotty Creek metasediments. Above the redox fronts, diamictites are variably weathered to ferruginous and bleached kaolinitic saprolites which are stable under oxidizing, circum-neutral conditions. Ferruginous diamictites are rich in recycled redox-sensitive elements derived from oxidation of ferromagnesian, sulfide and opaque oxide heavy minerals. These weathering features can be used to identify weathered diamictite for sampling for hydromorphic metal dispersion studies.

1. Introduction

Many regions of the world are covered by thick, residual and transported regolith or young Phanerozoic sedimentary rocks (Cohen & Bowell, 2014). Transported cover generally refers to exotic or redistributed material of continental origin that blankets weathered and fresh bedrock and sometimes cemented by Fe oxides, silica or carbonates (Anand & Paine, 2002; Butt et al., 2008). Regolith-dominated terrains covered by transported regolith include the Permo-Carboniferous to Quaternary sedimentary basins of Australia, colluvial and alluvial basin fill in the southwestern United States and the Andes, recent volcanic ash in modern volcanic arcs such as Indonesia, and glacial deposits across Australia, Canada, northern USA, China, Fennoscandia, and Russia (e.g. Wang et al., 1999; McClenaghan et al., 2000; Averill, 2001; Lehtonen et al., 2005; Anand & Robertson, 2012;

* Corresponding author at: CSIRO, Mineral Resources Flagship, 26 Dick Perry Avenue, Kensington WA 6151, Perth, Australia.

http://dx.doi.org/10.1016/j.oregeorev.2015.07.014
0169-1368/

Cohen & Bowell, 2014) . Some of these regions are underexplored relative to their potential for hosting economic mineral deposits.

Transported cover is a frustrating impediment to mineral exploration because it masks the detectable signature of buried mineral systems and dispersion of indicator elements to the surface (Butt et al., 2000; Anand, 2005; Anand & Butt, 2010; Salama et al., 2015). Transported cover is either restricted or is masked by past and/or present geochemical and mechanical processes unrelated to mineralization (Anand et al., 1997; Anand & Robertson, 2012). However, geochemical dispersion haloes and mineralogical changes within transported cover above deeply buried mineral deposits in such regolith settings have been documented (Mann et al., 1998; Smee, 1998; Lawrance, 1999; Wang et al., 1999; Anand & Paine, 2002; Kelley et al., 2003; Cameron et al., 2004; Butt et al., 2005; Anand & Butt, 2010; Anand & Robertson, 2012; Cohen & Bowell, 2014). Thus, there is a need to develop a new perception of cover as an exploration opportunity rather than an impediment. Glaciated terrains are a specific example of areas with transported cover. Till is the favored sampling medium in the glaciated terrains of the Northern hemisphere, particularly in northern USA, Canada, and Fennoscandia (e.g., McClenaghan et al., 2000, 2013; McMartin & McClenaghan, 2001; Lehtonen et al., 2005). Glacial geology has been much more thoroughly integrated into mineral exploration protocols in Finland and Canada (Shilts, 1984; Hirvas, 1989; Klassen, 1997) and have recently attracted the attention of Australian scientists (e.g., Anand & Robertson, 2012). Subglacial erosion of mineralization can produce a dispersion train defined by till geochemistry and indicator minerals (e.g., Levson, 2001; Averill, 2001; McClenaghan, 2005). Metal-rich debris is mechanically dispersed by glaciers and the resulting till more closely reflects the primary composition or endogenic components of the bedrock source than do regolith materials in other terrains (e.g., McClenaghan et al., 2000; McClenaghan & Kjarsgaard, 2001; Kjarsgaard et al., 2004; Lehtonen et al., 2005). Therefore, detailed analysis of till stratigraphy, ice flow direction and reconstruction of paleotopography is required as a basis for both sampling and data interpretation.

In Australia, mineral deposits are obscured by a thick regolith of deeply weathered rocks, commonly with an overlying cover of sediment and soil materials. The weathering framework and paleoclimatic variations of the Yilgarn Craton in southwest Australia can be summarized in five stages (Anand & Butt, 2010) namely: (1) glacial erosion during the Permo-Carboniferous and the deposition of Paterson Formation, followed by periods of rapid burial and denudation from the early Permian to the early Cretaceous (Weber et al., 2005); (2) late Cretaceous-mid-Tertiary humid and sub-tropical conditions which promoted intense chemical weathering and deeply weathered regolith (Pilland, 2007); (3) late Cretaceous-middle Eocene sea-level changes which resulted in erosion and formation of deep valleys; (4) middle to late Tertiary weathering under seasonally humid and tropical to subtropical conditions that resulted in intense alteration and weathering of Pre-Tertiary, Eocene sediments and the underlying bedrocks; and (5) late Tertiary and Quaternary changes in climatic conditions from arid to semi-arid that have caused instability and erosion of the land surface. These changes have impacted the sedimentation and weathering environments and increased ground water salinity in many areas (Anand & Paine, 2002).

Recently, mineral exploration in Australia has been progressively focussed on areas of deep transported cover (>30 m) as more easy areas become exhausted. Given the cost of deep drilling, high density sampling of weathered basement beneath the unconformity is not cost-effective. Instead, new exploration tools are required for mineral exploration of ore deposits buried deep under this cover. Heavy indicator mineral methods have not been applied in detail for provenance studies and mineral exploration in Australia, as they have been elsewhere (Mange & Wright, 2007; Sevastjanova et al., 2012), particularly in glaciated areas (e.g., Averill, 2001, 2011; Lehtonen et al., 2005; Sarala & Peuraniemi, 2007; Sarala et al., 2009; Eppinger et al., 2013). Post-depositional, hydromorphic metal dispersion of the weathering products from mineral deposits is another possible indication of the presence of mineralization (Rose et al., 1979; Anand & Robertson, 2012). Accordingly, we have undertaken a systematic stratigraphic, mineralogical and geochemical study to determine whether the Permo-Carboniferous diamictites in the Agnew–Lawlers gold province, Western Australia have properties that may help to identify mineralization in the underlying rocks.

2. Geological setting

2.1. Regional geology

During the late Paleozoic (late Carboniferous–early Permian; ca. 320–280 Ma), Australia was a part of the Gondwana Supercontinent. The Gondwana Supercontinent was extensively covered by large continental ice sheets. Evidence for glaciation in Australia includes diamictites and glacially striated bedrock surfaces at the northeastern coast of Kangaroo Island, South Australia (Bourman & Alley, 1999), Bacchus Marsh, Victoria, Wynyard, Tasmania, and a number of sedimentary basins and sites in the northern part of Western Australia (Crowell & Frakes, 1971). The Western Australian Shield (i.e., the Yilgarn and Pilbara Cratons combined, Fig. 1A) is made up of Archean and Proterozoic rocks (Wilde et al., 2001) and contains an extensive sedimentary record of late Paleozoic glaciation preserved in several sedimentary basins that flank it (Crowell & Frakes, 1971; Eyles et al., 2002). Early Permian ice centers were located on the Yilgarn Craton and the Pilbara Craton in Western Australia (Crowell & Frakes, 1971). When the ice melted at the end of Paleozoic, the glaciated upland was left with relict glacial deposits, and the peripheral, intracratonic basins (e.g., Canning, Carnarvon, Collie and Perth Basins) on all sides were filled with a thick succession of glacial deposits (Veevers, 1990; Eyles et al., 2002; Veevers et al., 2005).

On the north and northeast margins of the Yilgarn Craton, late Paleozoic sedimentary sequences are mostly deeply weathered and occur buried in scattered, glacially-eroded valleys beneath the Tertiary and Quaternary sediments (e.g., Anand & Paine, 2002; Anand & Butt, 2010). The Permo-Carboniferous sedimentary succession was studied in open mine pits and attains variable thicknesses up to 80 m at Laverton (Eyles & de Broekert, 2001), up to 50 m at Ockerburry Hill 30 km south of Bronzewing Gold Mine (Anand & Butt, 2010) and 10 to 20 m thick at Lancefield South Gold Mine (Anand & Robertson, 2012). Eyles and de Broekert (2001) identified glacial diamictites in glacially-eroded valleys at Laverton area with characteristic striated, 'bullet-shaped' and faceted clasts typical of sub-glacially transported materials. However, they were not able to determine the preferred direction of clast orientation, and thus described diamictites as 'unorganized'. It is suggested that the general ice flow direction in the southern part of the WA shield was toward the southeast direction (see Fig. 2, Eyles & de Broekert, 2001).

2.2. Local basement geology

The Agnew–Lawlers District lies approximately 300 km northwest of Kalgoorlie in the northern part of the greater Norseman-Wiluna Greenstone Belt in the northeast Yilgarn Craton (Fig. 1A). The district is highly mineralized with gold and nickel. The Yilgarn Craton consists of Archean granites, granitic gneiss and extensive northwest oriented, elongate greenstone belts (Williams, 1975; Myers, 1997). The regional stratigraphic architecture of the Agnew–Lawlers area was studied by Krapež et al. (2008), Squire et al. (2010) and Jowitt et al. (2014) and is summarized below

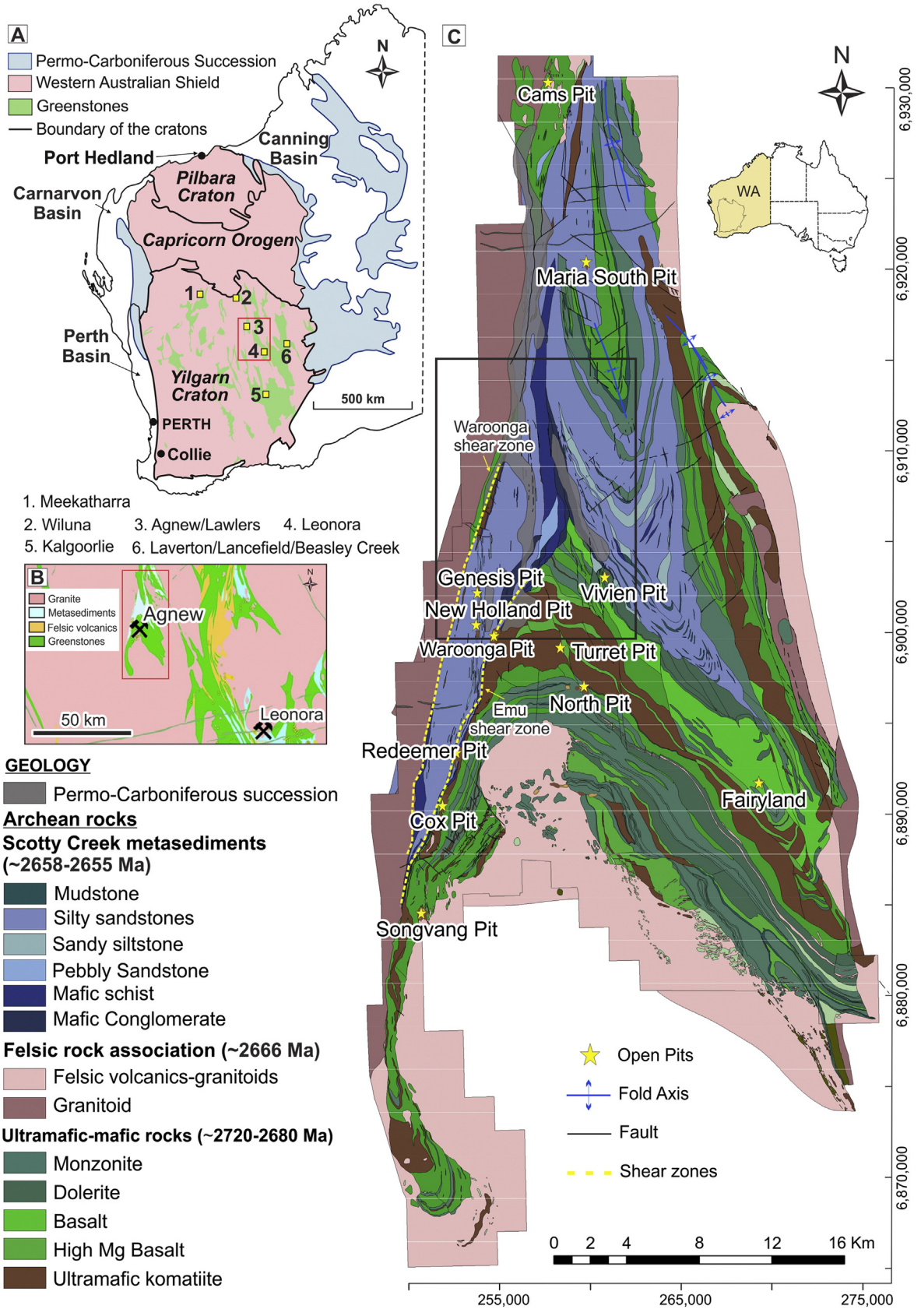

Fig. 1. A) A geologic map of Western Australia showing the Western Australian Shield (WAS) including the Yilgarn and Pilbara cratons and the surrounding sedimentary basin containing the Permo-Carboniferous glacial sediments (modified after Eyles & De Broekert, 2001 and Eyles et al., 2002). A small box refers to a close-up view in (B). B) A close-up view of the showing the Agnew–Lawlers area and main Archean rocks in the Yilgarn Craton. C) A geologic map of the Lawlers Anticline (box area in B), provided by Gold Fields Ltd., showing the distribution of the basement rock units and Permo-Carboniferous sediments in the region. (For interpretation of the references to color in this figure legend, the reader is referred to the web version of this article.)

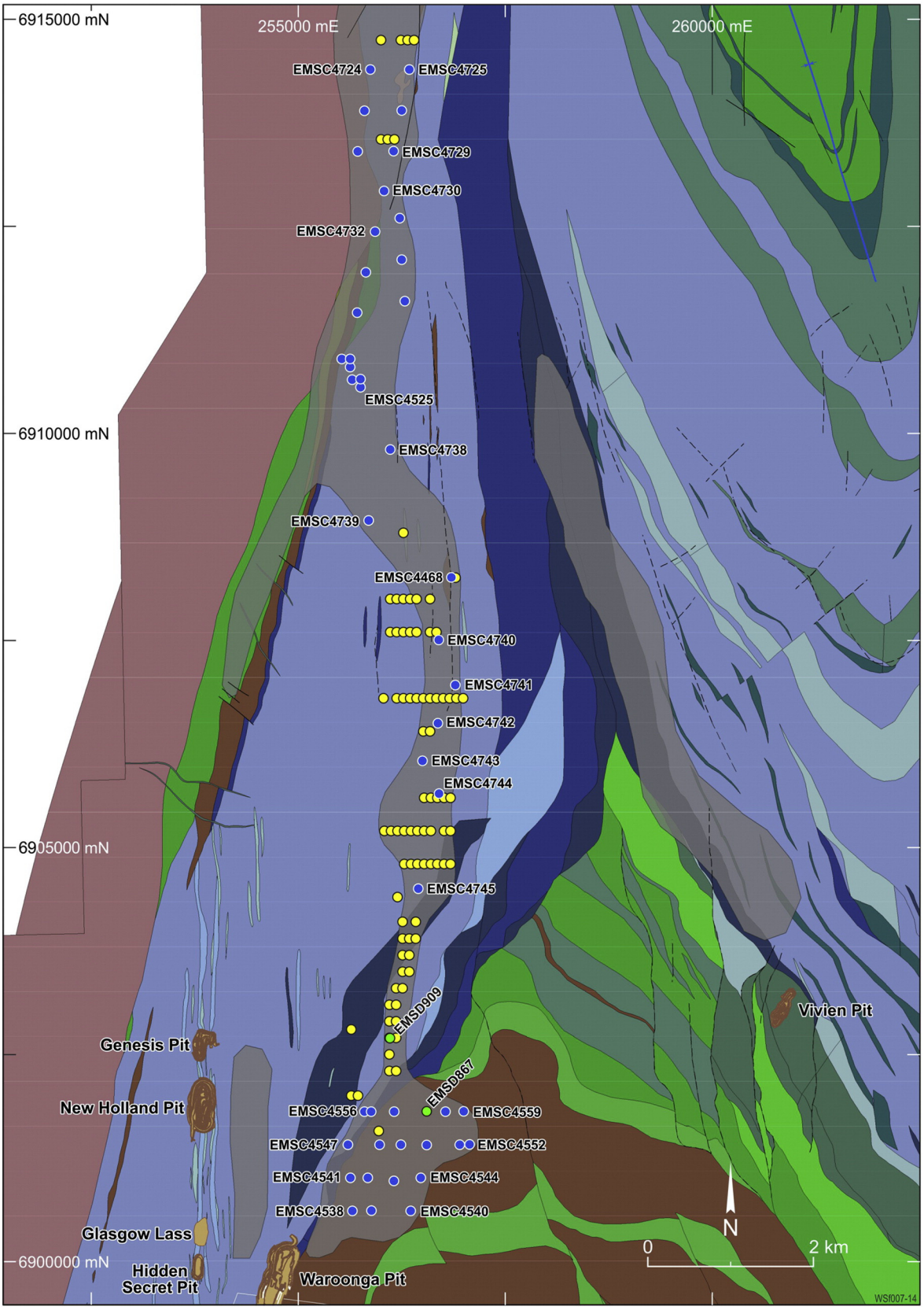

Fig. 2. A geologic map of Agnew–Lawlers area, provided by Gold Fields Ltd., showing the distribution of the basement rock units and the Permo-Carboniferous glacial sedimentary sequence as well as the location of the reverse circulation (RC, blue color), diamond drill (DD, green color) and air core (AC, yellow color) holes. (For interpretation of the references to color in this figure legend, the reader is referred to the web version of this article.)

from these sources. The greenstone belt (Kambalda sequence, Squire et al., 2010) consists of a mafic (Mg-basalt and gabbro) and komatiitic ultramafic sequence with quartzite, banded iron formation and minor felsic volcanic rocks (Platt et al., 1978). This succession is overlain by mafic and ultramafic conglomerates and capped by the Scotty Creek metasediments (Late Black Flag Group, Squire et al., 2010), which consists of sequence of polymictic, volcanic conglomerates dominated by mafic clasts with lesser felsic clasts interbedded with sandstones and siltstone.

The Agnew–Lawlers gold camp consists of a moderately tightly folded greenstone belt that is separated from an adjacent granite–gneiss terrane to the west (Fig. 1B) by the Waroonga Shear Zone (Fig. 1C), a 2 km wide dextral strike–slip zone associated with intense ductile deformation (Jowitt et al., 2014). The granitic rocks are deformed and metamorphosed granodiorite–tonalites. The Waroonga shear zone is a major regional-scale feature that defines the western edge of the Kalgoorlie Terrain (Liu et al., 2002). The center of the Agnew–Lawlers gold camp is dominated by the Lawlers Anticline, a large regional antiform that plunges 50°–60° to the north (Platt et al., 1978) and forms the locus of gold mineralization in the area (Fig. 1B). This anticline formed during progressive deformation associated with regional ENE–WSW-oriented contraction that caused reverse shearing, flexural slip on fold limbs and the development of shear zones with axial planes parallel to the associated fold-hinges. The core of the Lawlers anticline is dominated by the 2666 ± 3 Ma Lawlers mafic-type granitoid batholith (Fletcher et al., 2001; Foden et al., 1984; Blewett et al., 2010; Champion & Sheraton, 1997).

The NNE–SSW trending Emu Shear Zone forms the faulted boundary between ultramafic and metavolcanic sequence on one hand and the Scotty Creek metasediments in the western limb of the Lawlers anticline on the other hand (Fig. 1C). This shear zone is associated with the majority of the high-grade gold deposits that define the Agnew–Lawlers Gold Camp, including, from north to south, the Waroonga, Redeemer, Crusader and Songvang deposits (Broome et al., 1998) (Fig. 1C).

Gold mineralization within these deposits is generally hosted by felsic to mafic sedimentary rocks that are near or within shear zones and faults or are along unconformities that separate metavolcanic and metasedimentary units (Cassidy & Hagemann, 2001).

3. Sampling and analytical methods

3.1. Sampling

The Permo-Carboniferous sequence at the Agnew Gold Mine was selected because it contains the complete record of unweathered and weathered diamictites in the Yilgarn Craton. A total of 47 reverse circulation (RC) and two diamond (DD) drill holes at the Agnew Gold Mine were logged and sampled. The Permo-Carboniferous diamictites were identified in 29 of the RC, and both of the DD drill holes (EMSD909 and EMSD867). In addition, 86 air core (AC) holes were drilled by Gold Fields Ltd. between the RC and DD holes to assess the continuity of the Permo-Carboniferous succession (Fig. 2). These AC drill holes did not reach the Permo-Carboniferous–Precambrian unconformity.

Overall, two hundred and one samples were collected from the different Permo-Carboniferous diamictite units, overlying Tertiary and Quaternary sediments, and underlying basement rocks. Seventy-nine samples from the two DD drill holes were collected on centimeter and meter scales (Appendix 1). Weights of samples analyzed range from 200 g to 400 g and were collected from 10 cm core materials of EMSD909 and EMSD867. Samples from each stratigraphic rock unit of the Permo-Carboniferous succession were collected from the 29 RC drill holes. Samples collected from RC holes are rock chips of approximately 200 g. The strategy of sample selection was to determine if there is evidence of lateral mechanical dispersal of clasts and grains with increasing transport distance from the source and the local, vertical chemical variations due to subsequent weathering. In addition, 16 RC drill holes were studied from the surrounding residual (in situ) saprolite developed directly on Archean basement rocks. The thickness and lithological characteristics of the Permo-Carboniferous diamictites were used to reconstruct the paleolandscape of the Permo-Carboniferous sequence.

3.2. Analytical methods

Petrographic examination of selected core samples and RC chips were carried out on polished thin sections using Zeiss Axio Imager and Nikon polarizing microscopes. Semi-quantitative mineralogical compositions were determined by X-ray diffraction (XRD) analysis on pressed powder samples using a Bruker D4 Endeavor operating with Co Kα radiation at a voltage of 35 kV and a current of 40 mA. X-ray diffraction patterns were collected from 5° to 90° using increments of 0.02° and a scan speed of 0.1 per second. The X-ray diffractograms were interpreted with X-plot software.

Scanning electron microscopic (SEM) analyses were performed on carbon-coated, polished thin sections of core samples using a Zeiss Ultra-Plus field emission gun (FEG) SEM coupled with a Bruker X-Flash energy dispersive X-ray (EDX) detector for elemental analyses. An accelerating voltage of 20 kV and a beam current of 3 nA were used.

Sample preparation for heavy mineral analysis includes sample crushing and sieving in CSIRO Labs and heavy mineral separation was carried out in the Western Geolabs, Perth. Twenty two samples with a total weight of each sample ranges from approximately 200 g to 500 g and grain size less 250 μm in diameter were selected from diamictites of the lower and middle chemostratigraphic units from 11 drill holes. These include six drill holes in the southern part (EMSD909, EMSD867, EMSC4539, EMSC4543, EMSC4549 and EMSC4557), three drill holes in the central part (EMSC4742, EMSC4743 and EMSC4744) and two drill holes in the northern part of the study area (EMSC4732 and EMSC4738). Heavy mineral recovery is recorded and ranges from 0.27 g to 10.5 g (Appendix 2). Total sample is wetted, attritioned and then sieved on 38 μm screen to remove silts and clay. The recovered materials are dried and weighted. The remaining product (between 38 μm and 250 μm) is weighed and stirred into glass separation funnels containing TBE (Tetra bromo ethane) with a specific gravity of 2.95. Heavy mineral sank at the base are drained into filter paper, washed with acetone and dried then weighed. Polished thin sections of the heavy mineral concentrates were investigated under optical and scanning electron microscopy. Identification of heavy minerals and semi-quantitative estimation of their abundance were obtained from EDX and elemental mapping of mineral concentrates in polished thin sections.

A total of two hundred and one samples were selected for whole-rock geochemical analysis. Seventy six samples were collected from core samples from drill holes EMSD867 and EMSD909 and the rest of samples was selected from rock chips of the RC holes (Appendix 1). Sample preparation and chemical analysis were undertaken at Ultra Trace (Bureau Veritas) Analytical Laboratories of Perth, WA. Each sample was dried and then pulverized to 70 μm with a LabTech Essa pulveriser with 100 cm^3 chrome free bowls. At every stage and between every sample, hot water and compressed air were used to clean the equipment to minimize contamination. A 0.15 g aliquot of each milled sample was digested in a Teflon vessel mounted on a hot box using a 4-Acid Digest (5 ml HCl, 4 ml HNO_3, 4 ml HF and 2 ml $HClO_4$). The sample was brought to dryness and then leached with another 5 ml of HCl and volumed to 25 ml with deionized water. The solution was then analyzed by an Inductively Coupled Plasma Agilent mass spectrometer (ICP-MS) and iCap 6000 series optical emission spectrometer (OES). For elements such as Au, Pt, Pd and Hg, the samples were digested in hot aqua regia for 1.5 h. An in-house soil standard (GLG302-2) was

Table 1
RC drill holes and their coordinates at Agnew area with a total thickness (in meters), thickness of each Permo-Carboniferous chemostratigraphic unit and the overlying Tertiary and Quaternary sediments.

Drill holes	Northing	Easting	Total thickness of cover (m)	Tertiary and Quaternary sediments (m)	Permo-Carboniferous sediments		
					Upper unit (m)	Middle unit (m)	Lower unit (m)
EMSC4538	6,900,610.0	255,654.39	85	Absent	0–3	3–20	20–85
EMSC4539	6,900,611.5	255,881.87	100	0–1	1–5	5–54	54–100
EMSC4540	6,900,610.4	256,357.71	60	0-6	6–12	12–53	53–60
EMSC4541	6,901,010.1	255,629.47	116	0–3	3–7	7–40	40–116
EMSC4542	6,901,010.0	255,839.68	116	0–3	3–5	5–43	43–116
EMSC4543	6,900,971.1	256,153.50	125	0–5	Absent	5–41	41–125
EMSC4544	6,901,010.4	256,479.75	59	0–11	11–15	15–52	52–59
EMSC4547	6,901,410.3	255,534.87	80	0–8	Absent	8–42	42–80
EMSC4548	6,901,410.2	255,980.46	156	0–7	7–17	17–50	50–156
EMSC4549	6,901,410.3	256,238.29	189	0–8	8–13	13–46	46–189
EMSC4550	6,901,406.2	256,549.89	109	0–6	Absent	6–45	45–109
EMSC4551	6,901,408.3	256,951.89	71	0–12	12–15	15–20	20–71
EMSC4552	6,901,412.1	257,068.94	54	0–16	16–18	18–38	38–54
EMSC4555	6,901,810.0	255,741.78	70	0–11	11–13	13–40	40–70
EMSC4556	6,901,809.8	255,880.37	91	0–13	Absent	13–43	43–91
EMSC4557	6,901,809.9	256,157.60	132	0–13	13–21	21–55	55–132
EMSC4558	6,901,810.0	256,779.06	94	0–8	8–13	13–27	27–94
EMSC4559	6,901,810.6	256,998.05	49	0–7	7–14	14–38	38–49
EMSC4725	6,914,395.0	256,292.14	83	0–20	20–25	25–83	Absent
EMSC4729	6,913,410.0	256,107.63	68	0–25	25–30	30–68	Absent
EMSC4730	6,912,928.3	256,036.87	78	0–21	21–26	26–50	50–78
EMSC4732	6,912,437.4	255,926.16	86	0–26	26–36	36–57	57–86
EMSC4738	6,909,804.3	256,110.86	52	0–17	17–24	24–52	Absent
EMSC4740	6,907,504.9	256,697.80	32	0–4	4–18	18–32	Absent
EMSC4741	6,906,960.0	256,895.00	66	0–4	4–13	13–53	53–66
EMSC4742	6,906,500.0	256,686.00	105	0–6	6–15	15–34	34–105
EMSC4743	6,906,044.7	256,501.16	128	0–8	8–13	13–32	32–128
EMSC4744	6,905,649.7	256,699.80	129	0–8	8–11	11–38	38–129
EMSC4745	6,904,500.0	256,450.42	40	0–2	2–14	14–40	Absent
EMSD 867	6,901,810.4	256,549.41	104	0–8	8–28	28–47	47–104
EMSD 909	6,902,680.1	256,150.68	92.4	0–13	13–25	25–69	69–92.4

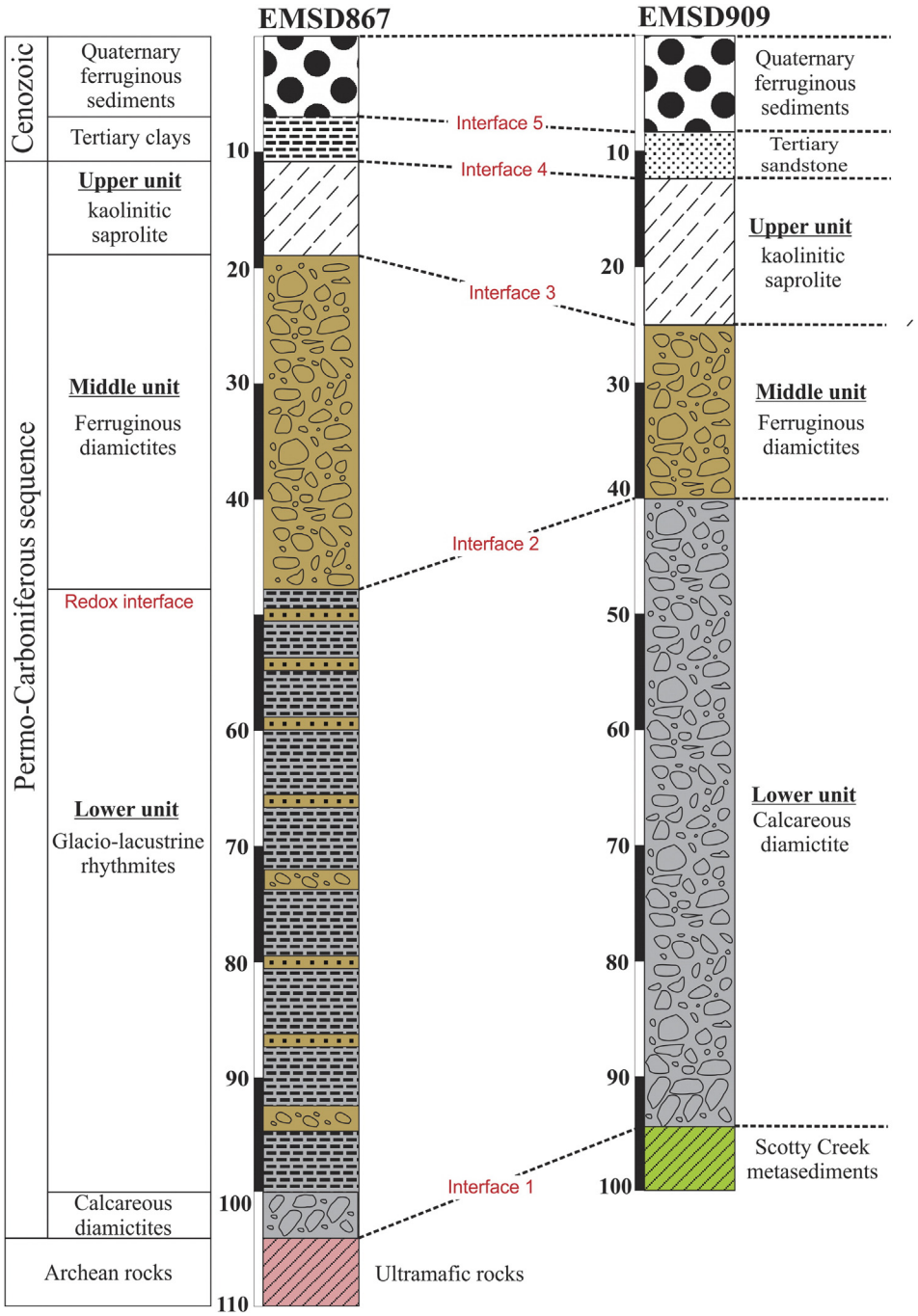

Fig. 3. Stratigraphic sections of Permo-Carboniferous sedimentary sequence of drill holes EMSD867 and EMSD909 showing the lateral facies changes from the glacially outwash gravelly sandstones and conglomerates (EMSD909) into glacio-lacustrine rhythmically laminated and interbedded siltstones, fine-grained sandstones and conglomerates (EMSD867). It also shows the three chemostratigraphic units (i.e., lower, middle and upper units) and the physical and chemical interfaces. The physical interface (interface 1) is represented by basal conglomerates that separate the basement from the Permo-Carboniferous sediments. The chemical interfaces include: 1) a redox interface (interface 2) separating the gray and calcareous sediments of the lower unit below water table from the ferruginous sediments of the middle unit above; 2) an interface 3 separates the middle unit from the overlying deeply weathered sediments of the upper unit; 3) an interface 3 separates the middle unit from the overlying Tertiary green clays; and 4) an interface 5 separates the Tertiary clays from the overlying Quaternary ferruginous sediments. (For interpretation of the references to color in this figure legend, the reader is referred to the web version of this article.)

used together with the laboratory standards (SARM1, 3 and 4 (Norite), Laterite 610-1, Gannet BM-21/310 and Canmet SU-1b) for calibration and drift correction; blanks and replicate analyses were used to determine precision and detection limits of ICP-MS/OES analyses. All results are presented in Appendix 1.

Carbon-coated polished thin sections were analyzed with a JEOL 8530F Electron microprobe at the Center for Microscopy, Characterization and Analysis (University of Western Australia). Operating conditions were 20 kV accelerating voltage and 10 nA emission current. Standardization was completed using specific reference minerals, including pyrite (for S), orthoclase (for K), jadeite (for Na, Al), corundum (for Al), SC olivine (for Si), spessartine (for Si and Mn), periclase (for Mg), Cr_2O_3 (for Cr), ZnO (for Zn), vanadium metal (for V), millerite and nickel metal (for Ni), Cobalt metal (for Co), magnetite (for Fe), niobium (for Nb), rutile (for Ti), $BaSO_4$ (for Ba), Durango apatite (for Ca and P).

The pH and electrical conductivity (EC) of the bulk samples of RC chips were determined using a powder sample to distilled water ratio

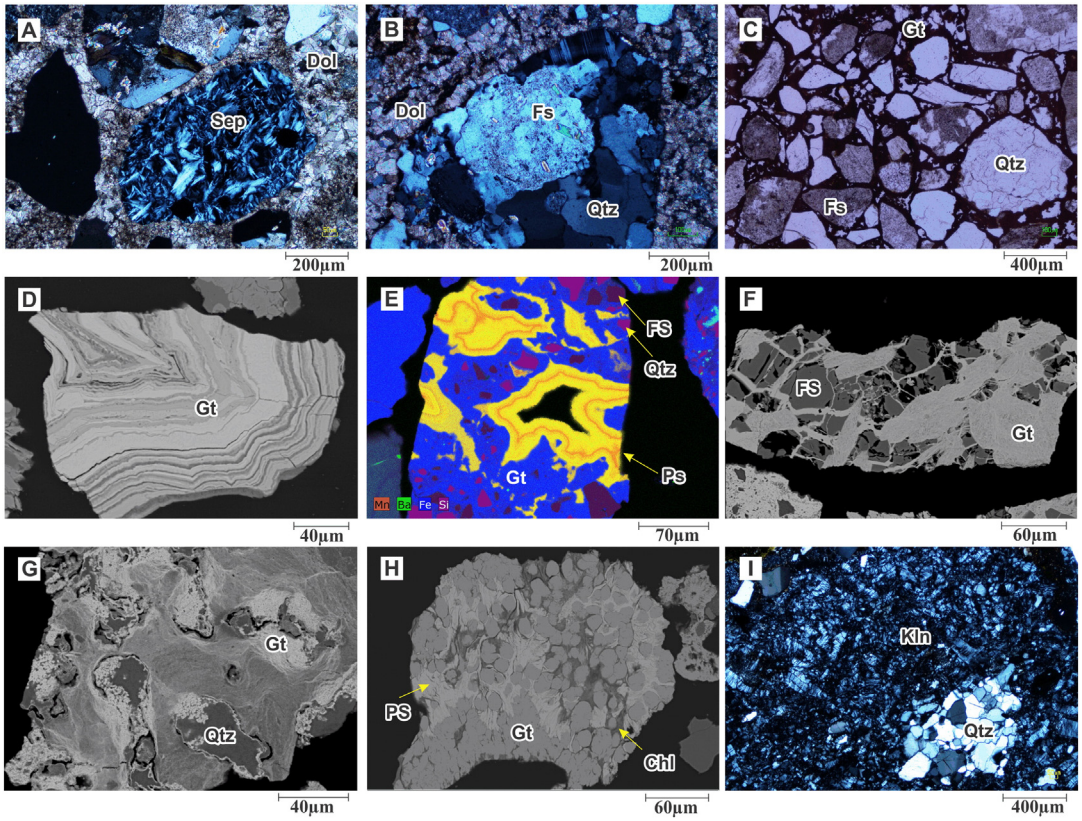

Fig. 4. Petrographic examination of the chemostratigraphic units. A) A photomicrograph showing an unweathered serpentinite clast (Sep) surrounded by well crystalline dolomite (Dol) cement (CN, EMSD867). B) A photomicrograph showing unweathered granitic clast that consists of quartz (Qtz) and feldspar (Fs) grains floating in turbid dolomite (Dol) cement (CN, EMSD867). C) A photomicrograph showing ferruginous sandstone consists of quartz (Qtz) and slightly weathered feldspar grains (Fs) cemented by goethite cement (PPL). D) A BSE image showing a fragment of colloform goethite (Gt) cement. E) An X-ray element map showing the ferruginous (blue color for Fe) and manganiferous (psilomelane, Ps) cements (yellow color for Mn and Ba) cementing quartz grains (red color for Qtz). F) A BSE image showing destruction and of feldspars (Fs) by goethite (Gt) cement. G) A BSE image showing a corrosion of quartz (Qtz) grains by ferruginous (Gt) cement. H) A BSE image showing the development of goethite (Gt) and psilomelane (ps) at the expense of chlorite (Chl) cement. I) A photomicrograph showing end products of weathering in the upper unit consisting of kaolinite (Kln) and quartz (Qtz). BSE image = back scattered electron image, CN = crossed nicols and PPL = plane polarized light. (For interpretation of the references to color in this figure legend, the reader is referred to the web version of this article.)

of 1:5 and this mixture was shaken up in plastic bottles for 15 min. The pH was measured with a TPS-900-P instrument and the EC was measured on a Cond 3210 instrument at CSIRO.

4. Results

4.1. Stratigraphic framework

At the Agnew gold mine, the Permo-Carboniferous sedimentary sequence extends from ~500 m northeast of the Waroonga Gold Mine in an approximately N-S direction for more than 14 km (Fig. 2). It unconformably overlies different Archean basement rocks including, from south to north, ultramafic and mafic rocks, Scotty Creek metasediments and granitoids (Fig. 2). In turn, they are unconformably overlain by the Tertiary and Quaternary sediments which constitute the present-day, broadly flat landscape. Detailed logging of 47 RC and DD drill holes showed that the Permo-Carboniferous sedimentary succession is present in only 31 RC and DD holes, while the other 16 RC holes intersected residual kaolinitic and ferruginous saprolites developed on Archean basement rocks. The depth of the basement/Permo-Carboniferous nonconformity varies from 32 m to 189 m and this creates a series of paleolows (basins) and paleohighs. Excluding the thickness of the overlying Cenozoic sediments, the Permo-Carboniferous succession in the Agnew–Lawlers District varies between 28 m to 181 m in thickness. The variation in thickness of the Permo-Carboniferous succession and the overlying Cenozoic sediments is presented in Table 1.

Facies analyses showed that the Permo-Carboniferous sedimentary succession is composed mainly of two continental, siliciclastic, and laterally intercalated lithofacies including diamictites, and glaciolacustrine rhythmites. Diamictites are generally massive with polymictic clasts floating in a matrix of sands, silts and clays. They may show a crude stratification at certain stratigraphic levels when intercalated with sandstone beds. Diamictites comprise more than 70% of the sequence in the central and northern parts of the study area. The polymictic clasts consist of mafic (basalt), ultramafic (komatiitic serpentinite), granite, gneiss, metasediments, metavolcanics, sulfide-bearing quartzite, banded iron-formation (BIF) and schist. The mafic, ultramafic, and BIF clasts have been extensively recorded mainly in the southern part of the study area. On the other hand, striated and facetted clasts of granite, gneiss, metavolcanics, sulfide-bearing quartzite, metasediments and metavolcanics are dominant in the central and northern parts of the study area. These clasts are rounded to subrounded when compared with the angular to subangular mafic, ultramafic, and BIF clasts.

Rhythmites consist of rhythmically, ripple cross-laminated and cross-bedded claystones, siltstones and fine-grained sandstones (Fig. 3). They comprise more that 70% of the sequence in the southern part of the study area. They consist of well sorted, grain-supported, subangular to subrounded, polymictic ferruginous sands and calcareous silts and clays. Clasts of siltstones are enclosed in the fine-grained sandstone bands of the rhythmite facies. The rhythmite facies contains gravelly sandstones beds with graded and cross-laminations. The rhythmite facies has a sharp and erosive contact with the overlying

Table 2
Representative chemical analyses of rhythmites in the southern part of the study area.

Sample nr.	WS4538-43	WS4539-83	WS4542-75	WS4543-69	WS4543-95	WS4544-57	WS4550-90	WS4556-69	WS4558-56
Depth (m)	43–44	83–84	75–76	69–70	95–96	57–58	90–91	69–70	56–57
Al_2O_3	12.11	12.47	12.43	14.64	13.04	13.00	12.11	13.30	12.85
Fe_2O_3	4.10	3.46	3.80	6.12	4.25	3.51	3.85	4.28	3.77
TiO_2	0.32	0.29	0.34	0.47	0.35	0.37	0.38	0.38	0.36
MnO	0.04	0.05	0.06	0.09	0.08	0.03	0.05	0.05	0.05
MgO	2.62	3.18	3.66	5.29	3.96	2.69	3.40	3.85	3.17
CaO	0.90	0.86	1.33	1.46	1.23	0.75	0.87	0.79	0.85
Na_2O	2.66	2.93	2.40	2.41	2.76	2.79	2.79	2.44	2.84
K_2O	2.89	3.02	3.40	3.79	3.46	3.57	3.61	3.58	3.18
P_2O_5	0.11	0.07	0.09	0.10	0.10	0.09	0.10	0.11	0.09
Au	3.00	2.00	3.00	4.00	1.00	1.00	2.00	2.00	3.00
Cr	170.00	245.00	165.00	180.00	180.00	180.00	135.00	160.00	135.00
Co	17.00	13.00	14.00	24.00	16.00	10.00	13.00	15.00	16.00
Ni	217.00	164.00	121.00	132.00	112.00	166.00	115.00	120.00	98.00
Cu	19.00	16.00	19.00	40.00	20.00	19.00	19.00	21.00	22.00
Zn	47.00	35.00	47.00	79.00	49.00	52.00	52.00	67.00	57.00
As	8.00	13.00	8.00	7.00	5.00	6.00	6.00	7.00	3.00
Pb	27.00	26.00	28.00	41.00	28.00	24.00	27.00	31.00	35.00
Sb	0.54	0.42	0.26	0.50	0.34	0.38	0.38	0.30	0.30
V	48.00	44.00	48.00	84.00	54.00	48.00	62.00	60.00	52.00
S	40.00	300.00	460.00	540.00	560.00	40.00	340.00	440.00	240.00
Li	25.60	25.60	39.80	47.80	39.00	24.80	34.60	44.20	37.80
Rb	118.00	118.00	140.00	177.00	136.00	152.00	152.00	142.00	138.00
Cs	3.90	2.90	5.10	8.70	4.70	6.60	6.40	5.50	4.80
Sr	173.00	179.00	150.00	140.00	160.00	165.00	174.00	140.00	158.00
Ba	711.00	681.00	754.00	745.00	767.00	776.00	745.00	790.00	787.00
Sc	7.50	6.50	8.00	12.00	7.50	8.00	8.00	8.50	7.50
Y	16.20	10.80	13.00	17.20	12.40	13.10	13.00	12.90	11.70
Zr	118.00	108.00	136.00	101.00	130.00	126.00	135.00	126.00	122.00
Hf	3.40	3.20	4.00	3.00	3.60	3.60	3.80	3.60	3.60
Nb	7.50	6.00	7.50	10.00	7.00	8.00	8.00	7.50	7.50
Ta	0.55	0.50	0.55	0.65	0.50	0.60	0.60	0.55	0.55
W	2.40	2.00	1.40	1.00	1.00	1.80	1.60	1.40	2.00
Th	17.10	13.20	16.30	25.50	15.80	17.00	15.60	16.90	15.70
U	4.10	2.05	2.50	6.40	2.00	2.00	4.15	2.75	2.00
LREE	188.88	130.02	128.78	157.29	119.11	121.90	128.62	125.87	110.08
HREE	7.36	5.10	6.10	8.18	5.75	5.93	6.17	5.77	5.35
LREE/HREE	25.66	25.49	21.11	19.23	20.71	20.56	20.85	21.81	20.58
ΣREE	196.24	135.12	134.88	165.47	124.86	127.83	134.79	131.64	115.43

diamictite and sharp and irregular contact with the underlying diamictites (boulder beds). The boulder beds are easily recognized when overlain by rhythmite (EMSD867, Fig. 3). The boulder beds consists of polymictic, boulder-sized clasts that are cemented by argillaceous and calcareous cements.

4.2. Chemostratigraphy and rock-forming minerals

The Permo-Carboniferous sedimentary succession is differentiated into three generalized chemostratigraphic units (lower, middle and upper units) based on the color, mineralogical composition, vertical chemical variations and degree of chemical weathering (Fig. 3). This subdivision did not take into considerations stratigraphic complexities in the glacial sedimentary succession arising from short-distant lateral facies changes between diamictites and rhythmites.

The lower chemostratigraphic unit unconformably overlies different Archean bedrocks and the unconformity is marked by a boulder bed, up to 4 m in thickness (Fig. 3, physical interface 1). This unit occupies the paleotopographic low areas and is mineralogically stable since deposition below the current water table under alkaline (pH = 8.2–9.4) and reducing conditions. Petrographic examinations of polished thin sections of the polymictic clasts and matrix components of the diamictites showed that they are heterogeneous in their mineralogical composition. The clasts and matrix components consist of ferromagnesian minerals (pyroxenes, amphiboles, serpentine minerals and biotite and chlorite), feldspars, muscovite and opaque heavy minerals. The mafic and ultramafic clasts are the main hosts of opaque sulfide and oxide heavy minerals (e.g., pyrite, chalcopyrite, pentlandite, chromite, magnetite and ilmenite). The polymictic clasts and matrix components and their mineralogical composition are unweathered in the lower unit (Fig. 4A and B). These framework components are cemented by argillaceous (e.g., chlorite and smectite), calcareous (e.g., dolomite (Fig. 4A and B), calcite, magnesite and ankerite) and/or pyritic cementing cements.

The middle and upper units represent the shallow part of the stratigraphic column that are stable above the current water table under a pH gradient from alkaline (pH = ~9.3) to circum-neutral (pH = ~7.2) and oxidizing conditions (regional redox interface 2). Petrographic examinations of polished thin sections showed that detrital rock-forming minerals of the polymictic clasts and matrix components of the diamictites are variably weathered, but still preserve the inherited sedimentary fabrics. Sulfide and ferromagnesian minerals have been altered to goethite, hematite and psilomelane which are the main components of ferruginous and manganiferous cements of the middle unit (Fig. 4C–H). Goethite, hematite and psilomelane occur as homogenous pore-filling phases, pseudomorphs after ferromagnesian minerals, colloform, fracture- and cavity-filling phases and replacement for quartz (Fig. 4C–H). Feldspars have been altered to sericite and kaolinite. All rock-forming minerals, except for resistate heavy minerals, have been completely weathered to kaolinite in the upper unit (Fig. 4I). The middle and upper units are commonly poorly indurated and the contact between them (interface 3) is either a sharp chemical interface marked by complete leaching of Fe and Mn oxides in the underlying unit, or is diffuse marked by kaolinite and hematite mottling. The Permo-Carboniferous sedimentary sequence changes laterally into deeply weathered (residual) kaolinitic and ferruginous saprolites that were developed on different basement rock units. The weathering front extends

Table 3
Representative chemical analyses of diamictites in the southern part of the study area.

Sample nr.	WS4540-60	WS4542-106	WS4543-124	WS4547-80	WS4549-188	WS4550-107	WS4551-69	WS4552-52	WS4558-93	WS4559-47
Depth (m)	60–61	106–107	124–125	80–81	188–189	107–108	69–70	52–53	93–94	47–48
Al_2O_3	11.64	11.66	11.90	12.47	11.39	10.37	9.83	10.22	9.54	10.22
Fe_2O_3	4.86	5.54	5.89	5.15	5.22	5.58	4.89	5.85	8.10	7.46
TiO_2	0.36	0.33	0.43	0.43	0.27	0.29	0.28	0.35	0.38	0.42
MnO	0.05	0.07	0.07	0.07	0.07	0.10	0.11	0.08	0.15	0.15
MgO	7.36	7.36	9.50	4.91	9.20	13.08	9.00	8.07	16.91	14.36
CaO	2.21	2.60	2.50	2.32	2.34	4.11	3.27	2.50	5.90	7.32
Na_2O	3.06	3.01	2.88	2.51	3.05	2.82	2.44	2.28	1.68	2.52
K_2O	2.05	2.41	2.40	2.40	2.37	1.71	2.10	2.25	0.99	0.60
P_2O_5	0.06	0.05	0.05	0.12	0.05	0.06	0.05	0.04	0.05	0.06
Au	1.00	14.00	4.00	3.00	3.00	1.00	3.00	4.00	2.00	<DL
Cr	500.00	410.00	800.00	575.00	665.00	1010.00	475.00	605.00	1490.00	1020.00
Co	30.00	31.00	40.00	30.00	35.00	46.00	27.00	32.00	67.00	57.00
Ni	409.00	364.00	472.00	297.00	459.00	640.00	481.00	862.00	790.00	630.00
Cu	19.00	22.00	21.00	41.00	37.00	18.00	37.00	36.00	26.00	76.00
Zn	45.00	45.00	55.00	73.00	87.00	56.00	61.00	50.00	56.00	59.00
As	5.00	24.00	12.00	17.00	11.00	7.00	2.00	4.00	9.00	35.00
Pb	18.00	22.00	18.00	26.00	22.00	16.00	15.00	15.00	9.00	8.00
Sb	0.82	0.78	1.14	0.38	0.92	1.86	0.68	0.82	0.96	1.86
V	62.00	62.00	82.00	88.00	68.00	72.00	62.00	76.00	120.00	116.00
S	180.00	400.00	780.00	260.00	280.00	660.00	380.00	60.00	280.00	80.00
Li	22.00	29.00	33.00	29.40	28.60	19.60	13.80	16.60	14.80	12.80
Rb	78.10	93.70	96.60	91.20	93.10	63.70	79.10	99.70	38.90	30.70
Cs	2.40	3.50	3.00	11.40	3.50	2.60	3.00	5.60	1.90	3.70
Sr	241.00	208.00	227.00	312.00	219.00	208.00	143.00	111.00	90.00	64.00
Ba	545.00	598.00	589.00	684.00	710.00	517.00	467.00	446.00	229.00	105.00
Sc	9.00	9.50	11.00	12.50	9.00	11.00	10.00	13.00	21.00	19.50
Y	9.40	10.30	10.80	11.50	8.55	7.95	11.60	13.10	9.35	11.20
Zr	75.40	80.60	57.80	146.00	59.90	61.40	82.20	75.80	38.10	47.30
Hf	2.20	2.40	1.60	5.40	1.80	1.80	2.20	2.40	1.20	1.20
Nb	3.00	4.50	4.00	4.00	3.00	2.50	3.00	4.50	2.00	2.50
Ta	0.25	0.30	0.20	0.30	0.25	0.25	0.25	0.30	0.15	0.15
W	0.60	1.00	1.40	2.20	2.00	0.40	1.20	2.80	1.60	1.00
Th	5.60	9.10	7.25	10.30	7.10	5.45	5.80	7.70	3.05	4.20
U	1.40	1.60	2.30	2.60	1.45	1.20	1.05	1.10	0.50	0.45
LREE	71.42	81.70	83.38	88.87	62.81	53.41	66.79	67.29	34.76	58.21
HREE	4.45	4.64	4.87	5.40	4.08	3.62	5.06	6.14	4.12	5.09
LREE/HREE	16.05	17.61	17.12	16.46	15.39	14.75	13.20	10.96	8.44	11.44
ΣREE	75.87	86.34	88.25	94.27	66.89	57.03	71.85	73.43	38.88	63.30

down to 65 m in depth and probably coincides with the current water table.

The upper unit of the Permo-Carboniferous sequence and the residual saprolite over basement rocks are difficult to distinguish from younger Cenozoic sediments due to erosive truncation (interface 4) by the Tertiary channel sands and clays and the overlying Quaternary ferruginous sediments (interface 5).

4.3. Whole-rock geochemistry

Chemical analyses in this section are presented to show geochemical variations between unweathered rhythmites and diamictites of the lower chemostratigraphic units and to show if there is any vertical hydromorphic dispersion of metals through the redox boundary between the lower unweathered chemostratigraphic unit and the weathered middle and upper chemostratigraphic units. Chemical analyses of all chemostratigraphic sedimentary and basement rock units and their weathering products are presented in Appendix 1. Representative chemical analyses of unweathered rhythmites and diamictites of the lower chemostratigraphic unit in the southern part of the study area are presented in (Tables 2 and 3). These analyses show pronounced chemical variations in the transition (e.g., Co, Cr, Cu, Ni, Sc, V, and Zn), HFS (e.g., Zr, Hf, Nb, Ta, Th and U) and REE (La–Lu) elements. Diamictites show higher concentrations in Ca, Mg and transition elements than rhythmites. In contrast, rhythmites show higher concentrations in HFS and REE elements than diamictites (Tables 2 and 3).

Plotting of Al_2O_3, FeO + MnO and CaO + MgO differentiated between Permo-Carboniferous chemostratigraphic units, Tertiary and Quaternary sediments, and the different basement rocks and their residual saprolite (Fig. 5A). The lower chemostratigraphic unit has a similar composition to the Precambrian Scotty Creek metasediments and a similar overlapping trend of CaO and MgO though less pronounced decrease in Na_2O and K_2O (Fig. 5B). Vertical chemical variations indicate that CaO and MgO together with FeO and MnO, are concentrating in several stratigraphic horizons dominated by sand- and gravel-sized clasts (Fig. 6). The concentrations of CaO and MgO are higher in diamictites in the southern part of the study area (Fig. 5A). Magnesium and Ca decrease upward from the lower to the upper unit. The weathered middle and upper units, Tertiary and Quaternary sediments and residual saprolites plot along the Al_2O_3–FeO + MnO axis with the ferruginous and manganiferous diamictite of the middle unit is enriched and aligned toward the FeO + MnO peak and the bleached kaolinitic upper unit toward the Al_2O_3 peak (Figs. 5A, 6). The middle chemostratigraphic unit clustered along Al_2O_3–K_2O + Na_2O axis, whereas the upper unit, together with in situ saprolite over basement rocks, is enriched in and plotted close to Al_2O_3 (Figs. 5B, 6). The correlation matrix discriminates between two different groups of elements (group 1 and group 2) that shows the distribution of trace and minor elements in the unweathered lower unit reflects variable source rocks and the polymictic nature of sediments (Table 4). Correlation coefficients between transition elements such as Fe, Co, Cr, Cu, Ni, Sc, V, and Zn show a strong positive correlation ($r = 0.5$-0.97, Table 4). Chromium, Co and Ni are strongly correlated with Mg, and slightly with Ca, whereas V and Sc are strongly correlated with Fe ($r > 0.9$, Table 4). There is also a strong positive correlation between Ti and V ($r > 0.7$). The correlation coefficients between high-field strength (HFS) elements, alkali and alkaline earth elements

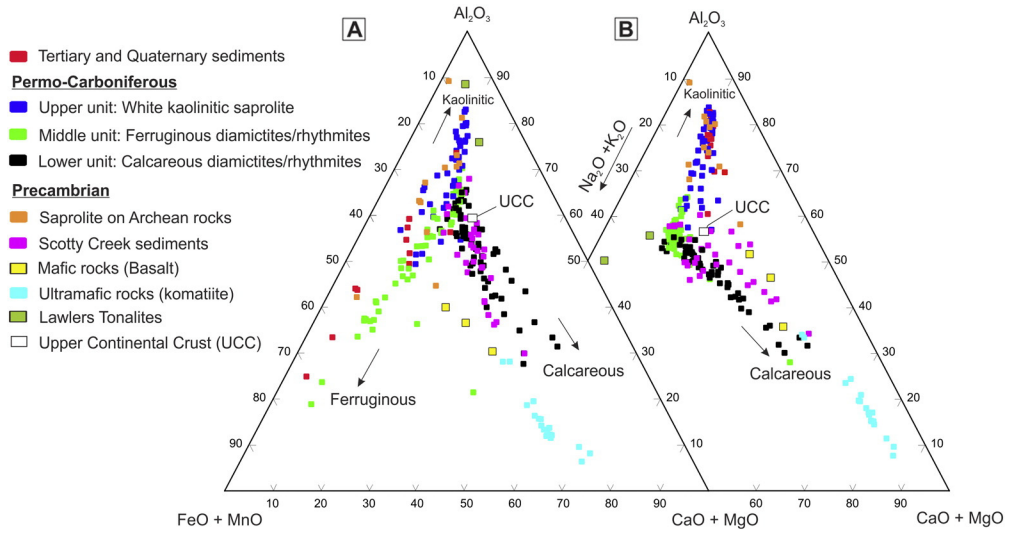

Fig. 5. Ternary diagrams A: (Al_2O_3/FeO + MnO/CaO + MgO) and B: (Al_2O_3/Na_2O + K_2O/CaO + MgO) show chemical variations between the different Permo-Carboniferous chemostratigraphic units, Tertiary and Quaternary sediments, different basement rock units including ultramafic, mafic, Scotty Creek metasediments and granitoids and the overlying residual saprolite. (For interpretation of the references to color in this figure legend, the reader is referred to the web version of this article.)

(e.g., K, Rb, Li, Be and Ba) and Al, Ga, P, Pb, Tl and LREE show a positive correlation (Table 4). This group of elements is negatively correlated with the transition elements and it reflects acidic igneous and metamorphic source rocks. There is also a strong positive correlation between Ca and Mn (r > 0.8) and Mg and Mn (r = ~0.6) and Sr and Na (r > 0.7). Strontium and Na show a negative correlation with Ca, Mg and Mn and a weak positive correlation with S (r = ~0.2). Sulfur increases (940–3020 ppm) toward the northern part of the study area. Higher

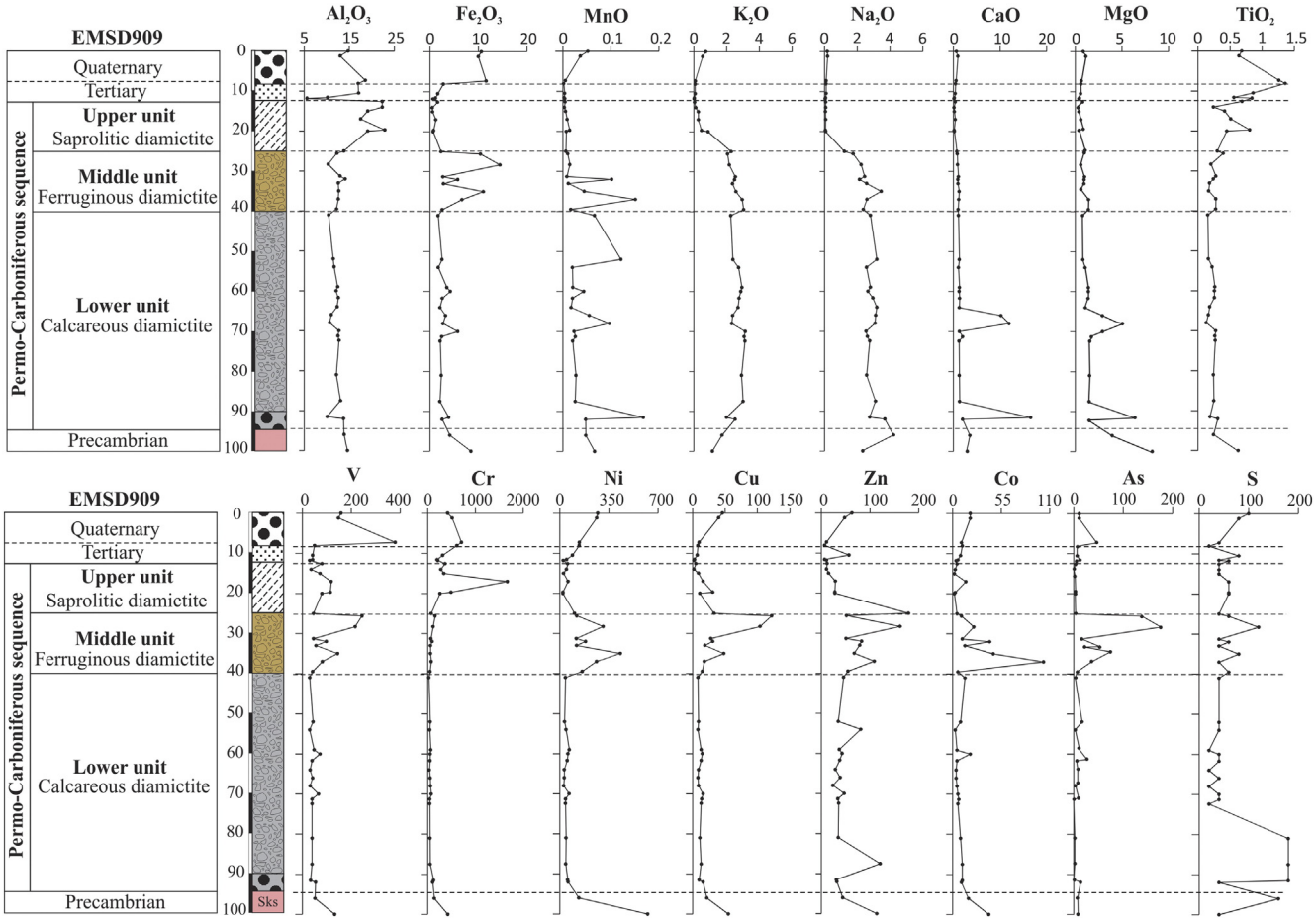

Fig. 6. Vertical chemical variations in major oxides (wt.%) and trace elements (ppm) content across different Permo-Carboniferous and Cenozoic stratigraphic units. (For interpretation of the references to color in this figure legend, the reader is referred to the web version of this article.)

Table 4
Correlation matrix showing positive correlation between Fe, Mg, Cr, Co, Ni, V, Cu, Sb and SC (group 1) and positive correlation between K, Ba, Ga, Li, Pb, Rb, Th, Tl, U, Zr, Be, Nb, Ta, Hf and LREE (group 2).

	Group 1 (mafic-ultramafic rock affinity)									Group 2 (felsic rock affinity)														
Element	Fe	Mg	Cr	Co	Ni	V	Cu	Sb	Sc	K	Ba	Ga	Li	Pb	Rb	Th	Tl	U	Zr	Be	Nb	Ta	Hf	LREE
Fe	1																							
Mg	0.85	1																						
Cr	0.83	0.95	1																					
Co	0.91	0.97	0.97	1																				
Ni	0.78	0.90	0.90	0.89	1																			
V	0.92	0.72	0.75	0.80	0.63	1																		
Cu	0.72	0.55	0.51	0.61	0.50	0.74	1																	
Sb	0.71	0.83	0.79	0.82	0.77	0.56	0.51	1																
Sc	0.92	0.76	0.79	0.83	0.70	0.97	0.75	0.58	1															
K	−0.50	−0.64	−0.71	−0.66	−0.63	−0.53	−0.36	−0.64	−0.58	1														
Ba	−0.62	−0.72	−0.73	−0.73	−0.69	−0.64	−0.54	−0.61	−0.72	0.84	1													
Ga	−0.34	−0.63	−0.67	−0.59	−0.69	−0.29	−0.24	−0.52	−0.38	0.83	0.80	1												
Li	−0.09	−0.17	−0.27	−0.14	−0.31	−0.01	−0.03	−0.15	−0.07	0.65	0.53	0.71	1											
Pb	−0.35	−0.60	−0.67	−0.55	−0.67	−0.34	−0.22	−0.53	−0.42	0.81	0.72	0.84	0.77	1										
Rb	−0.43	−0.62	−0.69	−0.63	−0.62	−0.43	−0.25	−0.61	−0.48	0.96	0.74	0.84	0.65	0.81	1									
Th	−0.20	−0.45	−0.53	−0.43	−0.50	−0.21	−0.03	−0.44	−0.25	0.85	0.57	0.77	0.75	0.84	0.90	1								
Tl	−0.51	−0.72	−0.74	−0.70	−0.69	−0.48	−0.36	−0.67	−0.55	0.90	0.83	0.87	0.60	0.86	0.89	0.79	1							
U	−0.09	−0.37	−0.39	−0.30	−0.38	−0.02	−0.02	−0.27	−0.09	0.52	0.37	0.60	0.50	0.64	0.57	0.63	0.57	1						
Zr	−0.52	−0.66	−0.63	−0.63	−0.63	−0.45	−0.19	−0.66	−0.46	0.73	0.61	0.56	0.40	0.58	0.72	0.69	0.66	0.33	1					
Be	−0.46	−0.72	−0.70	−0.67	−0.65	−0.42	−0.36	−0.57	−0.48	0.74	0.70	0.76	0.42	0.68	0.77	0.69	0.80	0.62	0.52	1				
Nb	−0.27	−0.54	−0.61	−0.52	−0.57	−0.25	−0.10	−0.52	−0.28	0.86	0.59	0.81	0.70	0.82	0.92	0.96	0.81	0.62	0.69	0.73	1			
Ta	−0.37	−0.56	−0.62	−0.57	−0.58	−0.34	−0.19	−0.55	−0.37	0.85	0.59	0.74	0.62	0.80	0.89	0.93	0.80	0.54	0.69	0.73	0.94	1		
Hf	−0.33	−0.53	−0.49	−0.47	−0.48	−0.27	−0.06	−0.53	−0.29	0.67	0.56	0.55	0.49	0.59	0.66	0.70	0.66	0.35	0.93	0.46	0.67	0.67	1	
LREE	−0.31	−0.51	−0.56	−0.48	−0.52	−0.32	−0.10	−0.45	−0.35	0.76	0.51	0.66	0.54	0.68	0.80	0.88	0.67	0.57	0.70	0.70	0.85	0.82	0.68	1

Table 5
Selected analyses of the EPMA of goethite, psilomelane, ilmenite, pseudorutile and rutile.

Mineral	Goethite				Psilomelane				Ilmenite				Pseudorutile				Rutile			
Sample ID	4732-2		4539-1	4744-2	4732-2				4743-1		4557-2	4738-2	4744-2		4738-2		4738-2			
SiO_2	4.43	3.74	6.86	3.04	0.88	1.50	0.43	0.11	bd	bd	bd	bd	bd	0.03	bd	0.17	bd	0.02	0.34	bd
Al_2O_3	0.02	bd	1.30	6.78	1.61	3.23	1.26	0.21	bd	bd	bd	bd	0.02	bd	bd	0.08	bd	bd	0.06	bd
$FeO_{(T)}$	78.40	73.96	67.44	77.04	0.31	0.51	2.78	1.20	44.22	43.99	43.79	40.22	42.03	37.56	22.53	4.07	1.12	0.84	0.70	0.49
MnO	0.22	0.14	0.53	0.19	61.37	57.90	54.89	58.45	1.99	1.56	1.36	8.39	5.55	9.46	0.14	6.72	0.01	0.02	0.02	bd
K_2O	0.02	0.01	bd	0.04	1.95	1.33	0.72	0.90	bd	bd	bd	bd	bd	bd	bd	0.01	bd	bd	bd	0.01
Na_2O	0.07	bd	bd	bd	0.56	0.23	0.14	0.56	bd	bd	bd	bd	bd	0.01	bd	bd	bd	bd	bd	bd
MgO	0.12	0.25	0.34	0.06	bd	bd	0.23	0.84	bd	bd	bd	bd	0.04	0.01	0.01	0.04	bd	bd	bd	bd
CaO	0.25	0.14	0.24	bd	0.04	0.07	0.40	0.55	bd	bd	bd	bd	bd	0.10	0.01	0.06	0.01	0.01	0.08	bd
TiO_2	bd	bd	bd	0.35	0.02	0.01	0.03	0.04	47.61	47.28	48.21	49.24	51.13	52.20	76.24	83.54	98.31	97.95	98.01	99.04
P_2O_5	0.76	0.42	0.09	0.10	bd	0.02	0.37	0.20	bd	bd	bd	bd	bd	bd	bd	0.07	bd	bd	bd	bd
SO_3	0.02	0.07	0.98	0.08	bd	bd	bd	bd	bd	bd	bd	bd	0.01	bd	bd	bd	bd	bd	bd	bd
V_2O_3	0.11	0.06	0.03	0.23	0.28	0.40	0.26	0.12	0.07	bd	bd	bd	bd	0.09	bd	0.14	0.18	0.14	0.03	bd
Cr_2O_3	0.07	0.04	0.11	0.36	bd	bd	bd	bd	bd	bd	bd	bd	bd	bd	bd	bd	bd	0.01	bd	bd
CoO	0.11	0.09	bd	bd	0.50	0.43	0.54	0.08	bd	bd	bd	0.08	bd	bd	0.01	0.03	bd	0.01	0.01	bd
NiO	bd	bd	bd	bd	bd	bd	0.25	0.08	bd	bd	bd	0.47	bd	bd	bd	0.01	bd	bd	bd	bd
ZnO	bd	bd	bd	bd	bd	bd	bd	bd	bd	bd	bd	bd	bd	bd	bd	bd	bd	0.01	0.01	bd
BaO	bd	bd	bd	bd	12.23	13.77	16.35	14.22	bd	bd	bd	bd	bd	bd	bd	1.60	bd	0.06	0.05	bd
Total	84.61	78.92	77.93	88.29	79.75	79.42	78.65	77.57	93.89	92.83	93.36	98.40	98.78	99.46	98.95	96.53	99.63	99.07	99.31	99.53

bd: below detection.

sulfur contents are associated with elevated electrical conductivities (EC) in the lower unit (940 μs/cm) when compared with low EC value in the upper unit (54.1 μs/cm).

The trace and minor elements such as As, V, Ni, Co, Cu and Zn increase in concentration in the middle unit. High concentrations of these elements are associated mainly with dissolution and reprecipitation of iron and manganese oxide (goethite and psilomelane) along the redox interface (Fig. 6). Correlation coefficients show a significant to strong positive correlation between Fe, Mn, Ni, Co, Cu, V, P ($r = 0.5–0.8$). Potassium shows a strong positive correlation with Rb, Cs, Ba, Th, Tl, Nb and Ta ($r = 0.5–0.9$). Manganese also shows a strong positive correlation with Ba ($r > 0.7$) and BSE images and elemental maps showed that Mn, Ba, K, Pb and Ce are the main constituents of the psilomelane and barite cements. Selected EPMA are shown in Table 6, but the average chemical composition of goethite ($n = 19$) shows a total FeO content (70.7 wt.%), SiO_2 (5.7 wt.%), Al_2O_3 (1.15 wt.%) and psilomelane ($n = 22$) consists of MnO (58.5 wt.%), total FeO (2 wt.%), BaO (13.5 wt.%) and Al_2O_3 (1 wt.%) (Table 5). Complete electron probe microanalyses (EPMA) dataset and structural formulae of goethite and psilomelane cements are presented in Appendix 3. BSE images and element maps show that Si, P and Ce are concentrated in colloform, cavity-filling, P-rich cerite and siliceous cements, which is associated with, but parageneticaly after, ferruginous and manganiferous cements. Calcium and Mg and Sr and Na show a positive correlation ($r > 0.9$) and are probably incorporated into carbonate, sulfate and halide cementing phases. Immobile elements such as Al, Sc, Ti and Ga show a positive correlation ($r = 0.6–0.9$) in the middle and upper units and hence similar conservative behavior during weathering. Titanium, Sc, Zr and Ga are immobile elements during weathering and they show nearly similar conservative behavior in all Permo-Carboniferous units. These elements together with a negative Ce-anomaly (Ce/Ce^*) increase across interface 4 between the Permo-Carboniferous and Cenozoic sediments.

4.4. Indicator heavy minerals

The Permo-Carboniferous sequence includes variable proportions of indicator sulfides (e.g., pyrite, chalcopyrite, arsenopyrite, and pentlandite), opaque oxides heavy minerals (e.g., chromite, magnetite and ilmenite) and non-opaque minerals (e.g., zircon, xenotime, apatite and monazite). These minerals vary in their abundance from south to north of the study area and occur either as free detrital grains in the matrix of diamictites or as hosted in different types of rock clasts. Mineral

Table 6
Selected analyses of the EPMA of chromite (inner chromite, middle ferritchromite, outer Cr-magnetite and Cr-goethite zones) and magnetite of BIF.

Mineral	Chromite core				Ferritchromite				Cr-magnetite				Cr-goethite rim				Magnetite (BIF)			
Sample ID	4743-1		4738-2		4743-1		4738-2		4743-1	4738-2		4539-1	4738-2				4743-1		4744-2	
SiO_2	bd	bd	bd	bd	bd	bd	bd	bd	bd	bd	bd	0.08	10.19	8.85	9.77	5.89	bd	bd	bd	bd
Al_2O_3	14.21	14.46	15.59	11.43	0.23	12.85	0.51	0.45	0.02	0.29	0.30	0.02	2.37	3.03	3.73	1.57	bd	bd	0.04	0.04
$FeO_{(T)}$	26.38	26.29	26.55	38.06	53.59	37.64	52.17	56.51	72.16	61.21	62.32	81.72	51.81	50.68	53.08	45.47	87.83	87.29	87.70	90.64
MnO	0.39	0.30	0.63	0.83	0.74	0.80	0.92	1.11	0.19	0.99	0.89	0.05	0.63	0.55	0.42	0.99	bd	0.02	0.06	0.09
K_2O	bd	bd	bd	bd	bd	bd	bd	bd	bd	bd	bd	bd	0.01	0.01	bd	0.02	bd	bd	bd	bd
Na_2O	bd	bd	bd	bd	bd	bd	bd	bd	0.01	bd	0.02	bd	bd	bd	bd	0.03	bd	bd	bd	bd
MgO	6.21	6.64	5.27	1.16	0.42	1.85	0.31	0.53	1.10	0.40	0.44	bd	0.56	0.59	0.69	0.44	bd	bd	bd	bd
CaO	0.02	bd	bd	bd	bd	bd	bd	bd	0.18	bd	bd	bd	0.20	0.18	0.13	0.11	bd	bd	bd	0.02
TiO_2	0.27	0.29	0.45	1.33	1.30	3.10	2.67	2.17	0.22	2.62	2.49	bd	1.70	1.89	1.41	2.92	bd	bd	bd	bd
P_2O_5	bd	bd	bd	bd	bd	bd	bd	bd	bd	bd	bd	0.03	0.19	0.24	0.14	0.04	bd	bd	bd	bd
SO_3	bd	bd	bd	bd	bd	bd	bd	bd	bd	bd	bd	bd	bd	bd	bd	bd	bd	bd	0.01	0.01
V_2O_3	0.09	0.09	0.18	0.48	0.05	0.19	0.17	0.15	0.07	0.15	0.16	0.03	0.19	0.18	0.16	0.23	bd	bd	0.15	0.21
Cr_2O_3	46.69	46.70	46.84	41.10	33.06	35.97	35.72	33.89	13.70	28.46	26.79	8.84	16.17	16.47	12.16	27.54	bd	bd	0.02	0.01
CoO	0.07	0.05	0.15	0.14	0.08	0.14	0.10	0.11	0.06	0.12	0.12	bd	0.09	0.09	0.08	0.13	0.01	0.03	bd	bd
NiO	bd	bd	0.07	0.05	0.11	bd	0.06	0.07	0.60	0.07	0.11	bd	0.08	0.09	0.06	0.06	bd	bd	bd	bd
ZnO	0.31	0.08	0.94	0.86	0.49	1.36	0.36	0.36	bd	0.26	0.24	bd	1.19	1.61	1.31	2.01	bd	bd	bd	bd
Total	94.63	94.90	96.65	95.44	90.08	93.90	92.99	95.35	88.32	94.58	93.88	90.70	75.19	75.61	73.38	81.56	87.83	87.35	87.98	91.02

bd: below detection.

Table 7
Summary of heavy mineral characteristics (size, shape and abundance) in the source rocks, unweathered and weathered diamictites.

Rock type	Range	Sulfides			Cr-spinel	Magnetite	Ilmenite	Monazite	Apatite	Zircon
		Pyrite	Chalcopyrite	Pentlandite						
Weathered diamictites	Abundance	2%	Absent	Absent	23%	37%	28%	5%	3%	2%
	Size (μm)	Few grains (135–230)	Absent	Absent	100–255	83–400	145–360	80–280	5–75	87–150
	Shape	Weathered to goethite	Absent	Absent	Anhedral grains	Euhedral to subhedral grains, equant and martitized	Prismatic grains, equant aggregate, weathered to anatase	Subhedral to anhedral grains, replaced by quartz, pitted and corroded	Anhedral and corroded grains	Equant grains, bipyramidal shape, zoned, corroded
Unweathered diamictites	Abundance	15%	1%	1%	18%	30%	25%	5%	3%	2%
	Size (μm)	110–310	90–220	25–90	55–310	178–360	140–420	130–290	10–90	55–165
	Shape	Detrital(euhedral (six-sided) to subhedral) and cements (colloform, framboids and zoned)	Anhedral grains and irregular aggregates	Zoned, equant aggregates and cavity-filling in monazite	Euhedral (six-sided) to subhedral grains, zoned and intergrown with amphiboles	Euhedral to subhedral grains and equant aggregates	Prismatic grains, exsolution, aggregate, altered to titanite	Subhedral to anhedral grains, zoned, rectangle, altered to apatite and filled with pentlandite	Anhedral grains, irregular aggregates and euhedral, six-sided	Equant grains and bipyramidal shape
Source rocks	Abundance	8–11%	1–3%	1–3%	0–20%	2–30%	3–23%	2–5%	1–3%	1–2%
	Size (μm)	112–583	60–235	125–420	125–325	90–410	90–425	210–380	10–175	45–175
	shape	Euhedral cubes and irregular aggregates	Anhedral grains and irregular aggregates	Anhedral grains and irregular aggregates	Euhedral (six-sided) to subhedral grains	Subhedral grains, elongated and equant aggregates	Prismatic grains, exsolution, aggregate, altered to titanite	Subhedral to anhedral grains, zoned, rectangle, altered to apatite	Anhedral grains and irregular aggregates	Equant grains, bipyramidal shape, zoned

Table 8
Heavy mineral abundance in the unweathered and weathered diamictites of selected drill holes from the northern, central and southern sectors of the study area. Magnetite is dominant in the lower unit and is oxidized into goethite in the middle unit. Goethite is also formed by weathering of other opaque heavy minerals.

Unit	Location	Sample ID	Depth (m)	Sulfides (%)	Cr-spinel (%)	Magnetite/ goethite (%)	Ilmenite/titanite/ anatase (%)	Monazite (%)	Apatite (%)	Zircon (%)
Middle unit (weathered diamictites)	Northern sector	EMSC4732-2	40–42	0	10	36	50	1	2	1
		EMSC4738-2	38–40	0	40	26	30	1	2	1
	Central sector	EMSC4744-2	28–30	2	3	65	30	2	7	1
		EMSC4743-2	24–26	2	10	40	35	5	5	3
	Southern sector	EMSC4557-2	42–44	2	13	20	57	2	5	1
		EMSC4549-2	34–36	2	17	46	23	5	5	2
		EMSC4543-2	36–38	0	5	74	15	2	3	1
		EMSC4539-2	44–46	0	10	29	50	6	2	3
Lower unit (unweathered diamictites)	Northern sector	EMSC4732-1	84–86	50	5	8	30	2	3	2
	Central sector	EMSC4742-1	103–105	42	3	13	32	5	2	3
		EMSC4743-1	118–120	34	5	13	33	8	5	2
		EMSC4744-1	100–102	50	5	11	25	3	5	1
	Southern sector	EMSC4557-1	110–112	23	11	30	29	1	5	1
		EMSC4549-1	180–182	24	23	11	33	1	7	1
		EMSC4543-1	123–125	10	40	25	20	2	2	1
		EMSC4539-1	98–100	12	12	18	54	1	2	1

chemistry of selected heavy minerals is presented in Tables 5 and 6. Identification of heavy minerals, characteristics (shape and size) and semi-quantitative estimation of their abundance in the diamictites and source rocks were obtained from EDX and elemental mapping of mineral concentrates in polished thin sections (Tables 7 and 8). Like the rock-forming minerals, heavy minerals in the lower chemostratigraphic unit are unweathered, but they show variable degrees of chemical weathering and alteration in the middle and upper chemostratigraphic units. Gold grains have neither observed in the diamictite clasts and matrix nor heavy mineral concentrates.

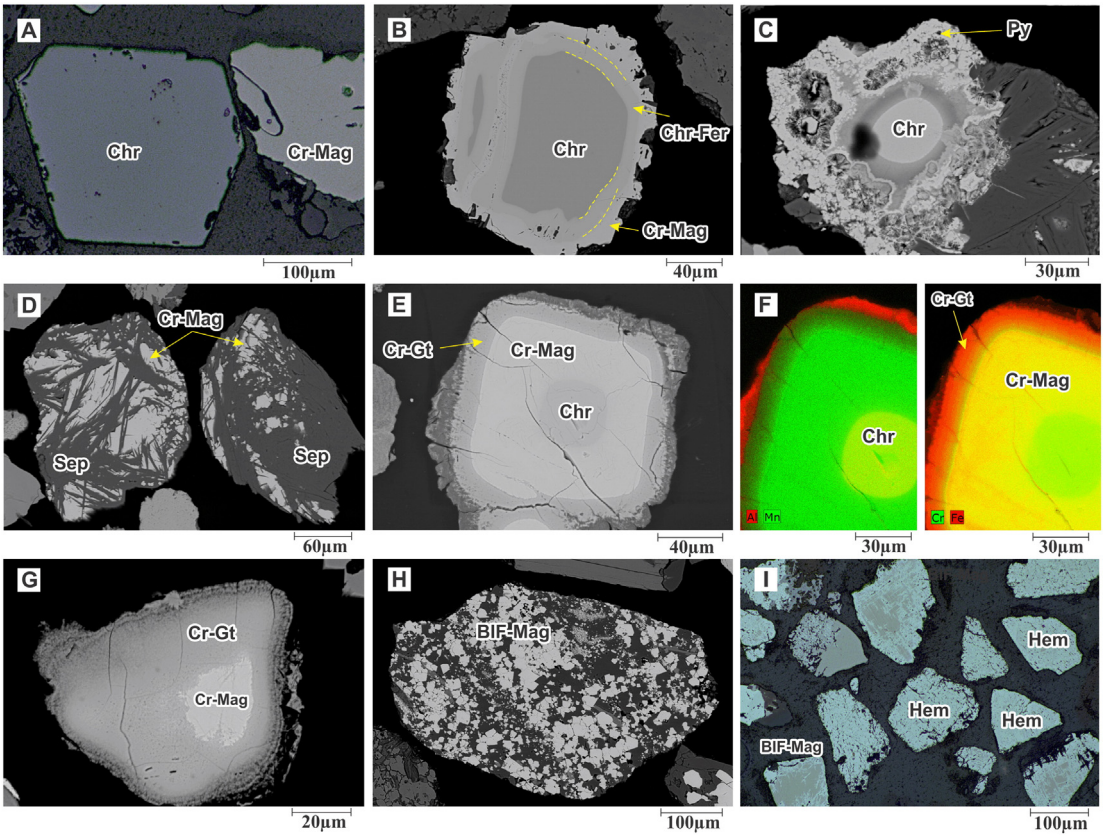

Fig. 7. Petrographic examination of Cr-spinel separated from the Permo-Carboniferous units as heavy mineral concentrates. A) A photomicrograph showing euhedral (six-sided), dark gray chromite (Chr) and light brown Cr-magnetite (Cr-Mag) grains, RL. B) A BSE image showing zoned Cr-spinel grains consisting of inner, dark gray chromite, middle light gray chromite-ferrit (Chr-fer) and outer Cr-magnetite (Cr-Mag) zones. C) A BSE image showing replacement of outer Fe-rich zone (s) of chromite (Chr) by pyrite cement (Py). D) A BSE image showing Cr-magnetite (Cr-Mag) in a fibrous serpentine mineral clasts (Sep). E) A BSE image showing zoned Cr-spinel grains is altered along the outer Cr-magnetite zone into Cr-rich goethite in the middle unit (EMSC4738). F) An X-ray element map showing the distribution of Cr, Fe, Al and Mn in a zoned Cr-spinel grain. G) A BSE image showing an advanced alteration of a Cr-magnetite (Cr-Mag) grain along its margin into Cr-rich goethite (Cr-Gt). H) A BSE image showing a clast of banded iron formation. I) A photomicrograph showing alteration of magnetite grains (Mag) into hematite Hem) through martitization process in the Middle unit. BSE image = back scattered electron image, CN = crossed nicols, PPL = plane polarized light, and RL = reflected light.

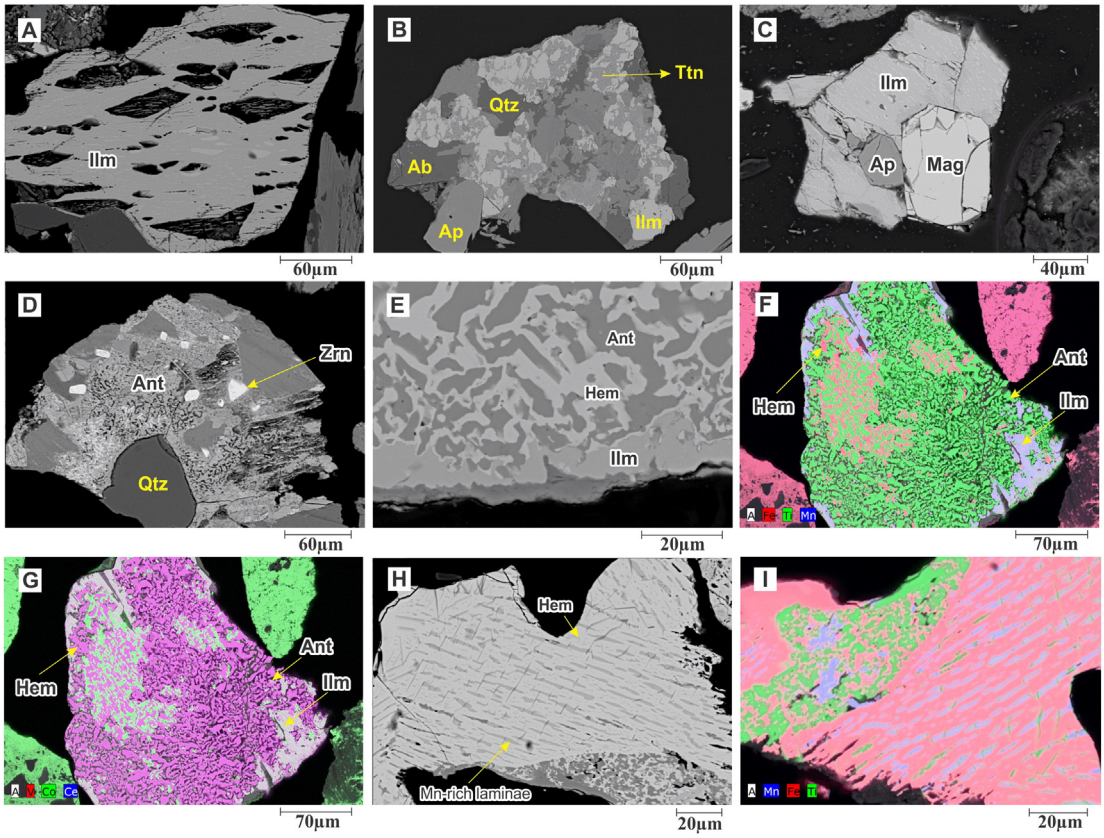

Fig. 8. Petrographic examination of ilmenite separated from the Permo-Carboniferous units as heavy mineral concentrates. A) A BSE image showing ilmenite grain (Ilm) with exsolved hematite laminae that are partially dissolved. B) A BSE image showing a clast containing ilmenite grains (Ilm) altered to titanite (Ttn), albite (Ab) and apatite (Ap). C) A BSE image showing a composite grain of ilmenite (Ilm), magnetite (Mag) and apatite (Ap). D) A BSE image showing an ilmenite grain altered to anatase (Ant) and contains inclusions of quartz (Qtz), zircon (Zrn). E) BSE image showing an ilmenite grain altered to anatase (Ant) and hematite (Hem) in a graphic-like texture. F & G) X-ray element maps showing the distribution of Fe, Ti and Mn in ilmenite, Ti, V and Ce in anatase (Ant) and Co in hematite (Hem). H & I) A BSE image (H) and an X-ray element map (I) showing hematite with exsolved Mn-rich ilmenite laminae. BSE = back scattered image. (For interpretation of the references to color in this figure legend, the reader is referred to the web version of this article.)

4.4.1. Cr-spinel (chromite–magnetite group)

Detrital Cr-spinel grains in polished thin section of heavy mineral concentrates are euhedral to subhedral, and their size rarely exceeds 250 µm in diameter (Fig. 7A, Table 7). They are dominant in unweathered diamictites in the southern part, and locally in the central part of the study area (EMSC4738, Fig. 2 and Table 8). Chrome spinel in the Permo-Carboniferous sedimentary sequence is mainly zoned with few grains lack internal zoning. Zoned chrome spinel grains show compositional variations in major and trace elements from the dark gray, inner magmatic chromite core to the outer metamorphic gray white, Cr-magnetite rim with a light gray ferritchromite center (Fig. 7B). Chrome spinel is resistant to weathering and alteration, however, in the lower chemostratigraphic unit the Cr-magnetite rims show replacement by the surrounding pyrite cement that may also fill cracks in the zoned chromite grains (Fig. 7C). The alteration normally observed as a "decolorization", has the form of irregular patches along the margins, cracks and cavities of the chromite grains. Contacts among the different zones in Cr-spinel are usually sharp, but occasionally not clearly defined and transitional. Chrome-magnetite grains are associated with pyroxenes and amphiboles with a characteristic interlocking texture (Fig. 7D). The Cr-magnetite rim of zoned chromite and Cr-magnetite grains show a gradual progression in alteration to Cr-goethite along peripheries or along cracks in the oxidation zone (Fig. 7E). Most of the altered Cr-spinel grains in the weathered diamictite of the chemostratigraphic unit are anhedral in shape. X-ray mapping shows chemical variations along the three different chromite zones (Fig. 7F and G) and the EPMA ($n = 14$) showed that Cr_2O_3 (average ~ 47 wt.%), Al_2O_3 (average ~ 13 wt.%) and MgO (average ~ 5.5 wt.%) and V_2O_3 (average ~ 0.2 wt.%) are enriched in the core (Table 6; Appendix 3). On the other hand, strong enrichment of total FeO (average ~ 76 wt.%) and NiO (average ~ 0.25 wt.%) is recorded in the outer Cr-magnetite ($n = 44$). The higher MnO (average ~ 1.2 wt.%), ZnO (average ~ 0.5 wt.%), CoO (average ~ 0.12 wt.%) and TiO_2 (average ~ 1.1 wt.%) values are always present in the ferritchromite zones ($n = 29$) and in the heterogeneous zones around the veinlets and the cracks in the case of the alteration. Weathering of the zoned chromite grains is mainly affecting the outer Cr-magnetite rim, whereas the inner chromite core and ferritchromite are stable. The Cr-magnetite rim is altered to goethite and this change is associated with enrichment in SiO_2 (average ~ 6.5 wt.%), Al_2O_3 (average ~ 2 wt.%), MnO (average ~ 1.2 wt.%), TiO_2 (average ~ 1.9 wt.%), CoO (average ~ 0.15 wt.%), ZnO (average ~ 1.2 wt.%) and V_2O_3 (average ~ 0.18 wt.%) (Fig. 7G, Table 6, Appendix 3).

In addition to the Cr-magnetite, pure magnetite and hematite clasts in the unweathered diamictites of the lower chemostratigraphic unit are derived from banded iron formation (BIF) in bedrock (Fig. 7H). Magnetite shows evidence of being stable under reducing condition in the lower unit, while hematite shows evidence of partial or complete dissolution. In the oxidation zone (middle and upper chemostratigraphic units), magnetite grains are altered along cleavage planes, margins and cracks into hematite (martite) or goethite in the oxidized zone (middle and upper units). Martitization involves alteration of magnetite to hematite which may be arranged in a pattern of intersecting lamellae (Fig. 7I). The EPMA showed that magnetite of the BIF largely consists of FeO (FeO: 85.7 to 92.4 wt.%) (Table. 6, Appendix 3).

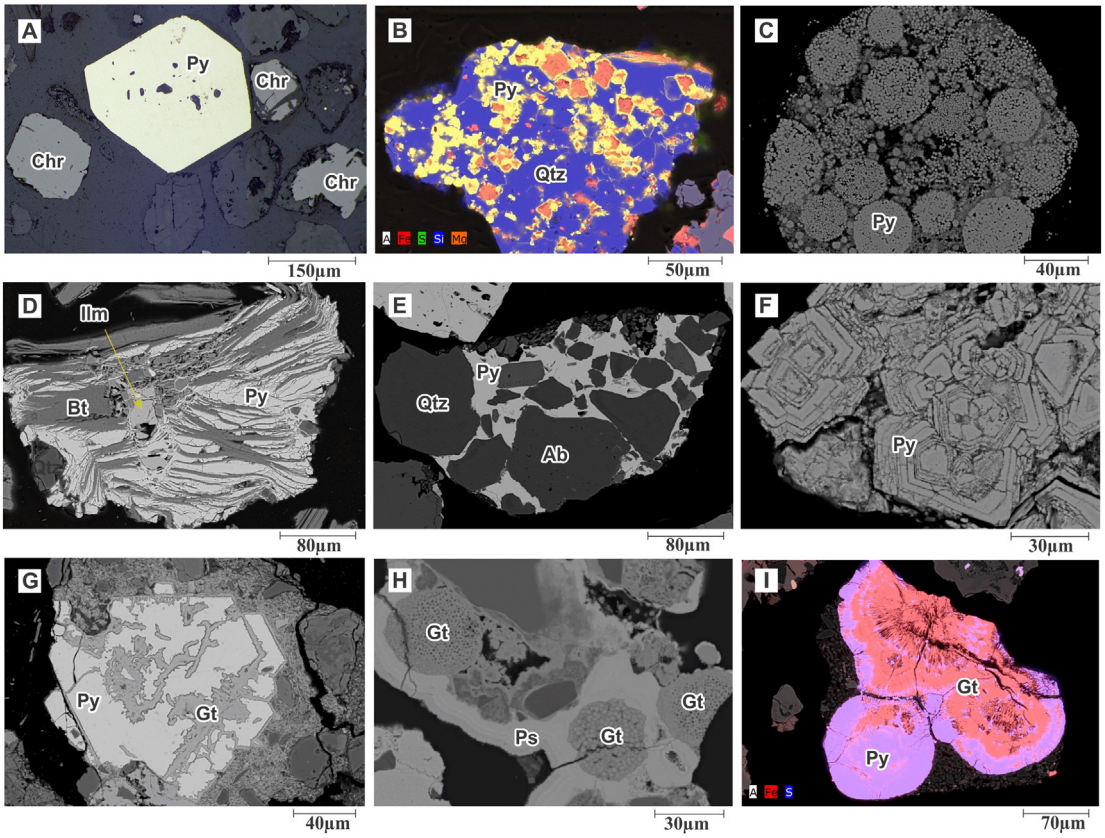

Fig. 9. Petrographic examination of different forms of pyrite from the lower Permo-Carboniferous unit as heavy mineral concentrates. A) A photomicrograph showing euhedral (six-sided), detrital pyrite grain, RL. B) An X-ray element map showing the distribution of Fe, S, Si and Mg in a pyrite-bearing quartzite (blue for Si) clast. Note the dissolution of pyrite cubes (yellow color for Fe and S) and their filling by chlorite (orange for Mg). C) A BSE image showing framboidal pyrite (Py) cement. D) A BSE image showing massive pyrite (Py) cement developed along the cleavage planes of biotite (Bt) and along fractures of ilmenite (Ilm). E) A BSE image showing massive pyrite (Py) cementing quartz (Qtz) and albite (Ab) grains. F) A BSE image showing zoned pyrite (Py) cement in the basal conglomerates in EMSD909. G) A BSE image showing partially altered pyrite (Py) into goethite (Gt). H) A BSE image showing goethite pseudomorphs after framboidal pyrite (Py) in psilomelane (Ps) cement. I) An X-ray element map showing the distribution of Fe in oxidized colloform pyrite cement. (For interpretation of the references to color in this figure legend, the reader is referred to the web version of this article.)

4.4.2. Ilmenite

Detrital ilmenite grains in diamictites are euhedral to subhedral, prismatic and equant in shapes, their grain size rarely exceed 400 µm and dominates in the study area. Two types of ilmenite grains have been identified in the unweathered diamictites below the redox boundary. The first is unweathered, fractured, and may show internal exsolved lamellae and blebs of Mn-rich hematite along cleavage planes (Fig. 8A). The second is altered along their margin into titanite and hosted in felsic and metasediment rock clasts together with quartz and feldspars (Fig. 8B) and contain inclusions of apatite and zircon (Fig. 8 C and D). The alteration products of the ilmenite retain the overall shape of the parent ilmenite, but internal textural features have been destroyed.

A selective dissolution of the exsolved Mn-rich hematite blebs from ilmenite is observed in ilmenite grains below the redox boundary (Fig. 8A). Ilmenite grains show variable degrees of alteration in the oxidation zone. Some grains show sieve texture, replacement structure and intergrowth of pseudorutile and anatase/rutile needles. The initial stage of ilmenite alteration includes removal of the Mn-rich hematite blebs and its transformation into intermediate mixture of hematite, pseudorutile and rutile/anatase (Fig. 8D–G). An ultimate stage of alteration is characterized by development of porous areas and includes removal of hematite and complete transformation into leucoxene and/or rutile/anatase. Kaolinite and quartz cement have been identified within the pores spaces created during the conversion of ilmenite to pseudorutile. The rutile/anatase displays epitaxial growth on the margin of ilmenite and a graphic-like texture. Few grains show exsolved Mn-rich ilmenite in hematite host (Fig. 8H and I). Selected EPMA are shown in Table 6, but the average chemical composition of the Mn-rich ilmenite ($n = 11$) shows a total FeO content (42.5 wt.%), TiO_2 (49.5 wt.%) and MnO (5.15 wt.%) (Appendix 3). The Ti/(Ti + Fe) ratio changes with progressive alteration of ilmenite (0.49–0.52) to pseudorutile and leucoxene (0.52–0.95) and finally to rutile/anatase (0.99–1.00) (Appendix 3). Complete EPMA dataset and structural formulae of ilmenite are presented in Appendix 3. Elemental maps showed that V and Ce are the main trace elements of the ilmenite that associated with Ti and Mn.

4.4.3. Sulfides

Sulfides are common as free detrital grains in matrix and hosted in rock clasts of the unweathered diamictites, and occur as secondary cavity- and fracture-fillings and framboidal pyrite cements (Fig. 9). Detrital sulfide consist mainly of pyrite, pyrrhotite, chalcopyrite and pentlandite with less frequent sphalerite, arsenopyrite and gersdorffite. Except for pentlandite, all of these sulfide minerals recorded mainly in the Scotty Creek metasediments and mafic conglomerates (Fisher et al., 2011). Pentlandite is recorded mainly in the ultramafic rocks and ultramafic conglomerates (Fisher et al., 2011). Pyrite grains in the unweathered diamictites are euhedral to subhedral, and their size rarely exceeds 350 µm (Fig. 9A; Table 7). They are hosted in clasts derived from pyrite-bearing quartz veins and abundant in the central part of the study area. Primary pyrite in these clasts is partially to completely dissolved and the dissolution cavities and boundaries between quartz grains are filled by secondary chlorite/smectite and pyrite cements (Fig. 9B).

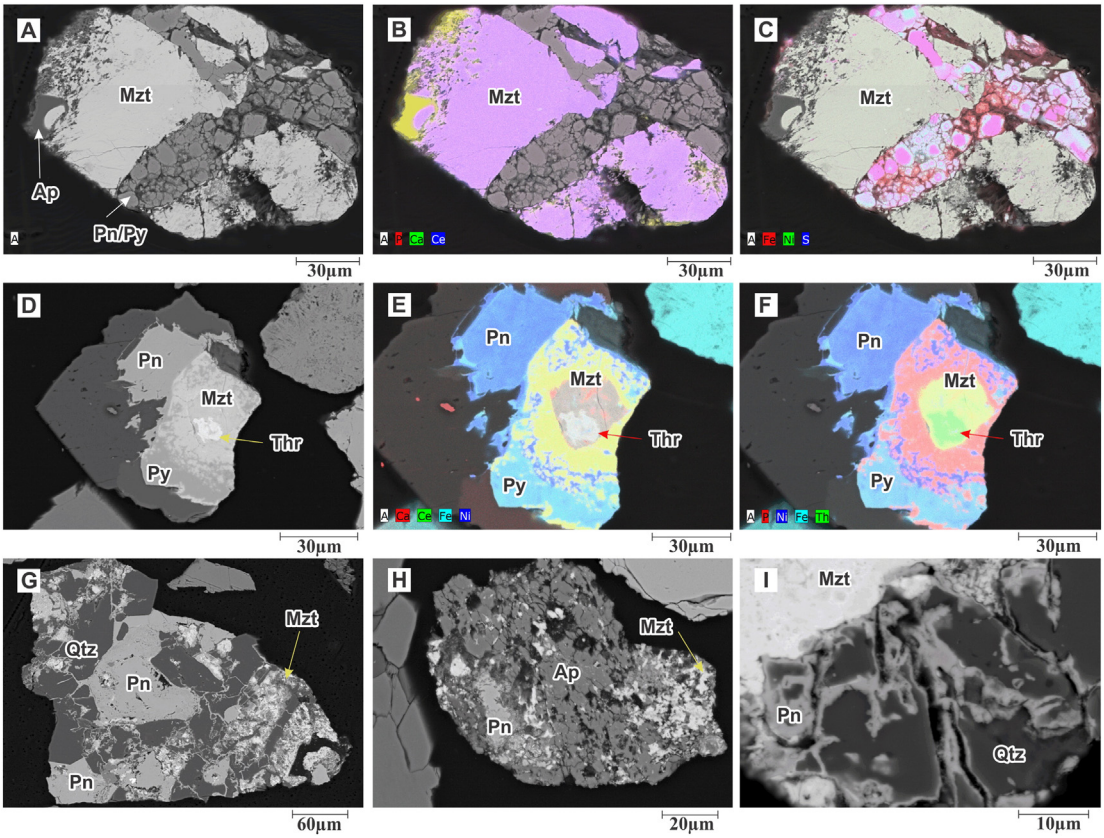

Fig. 10. Petrographic examination of Fe and Ni sulfides in the lower unit in the southern part. A–C) A BSE image (A) and X-ray element maps (B & C) showing cavity-filling, zoned pyrite-pentlandite veins cutting across partially altered monazite (Mzt) grain. Note the growth of apatite (Ap) at the margin of monazite (Mzt) grain. D–F) A BSE image (D) and X-ray element maps (E & F) showing monazite (Mzt) grain replaced by Fe and Ni sulfides along the margin and thorite (Thr) in the inner core. G) A BSE image showing a rock clast consisting of altered monazite (Mzt) and quartz (Qtz). Iron and Ni sulfides are replacing monazite and precipitated in cavities and along fractures cutting and corroding quartz grains. H) A BSE image showing a monazite (Mzt) grain replaced by apatite (Ap) and pentlandite (Pn). I) A BSE image showing pentlandite (Pn) corroding and replacing quartz grains (Qtz).

Pyrite cement dominates in the lower chemostratigraphic unit which is below the redox boundary and is common in the central and northern parts of the study area (Table 8). Pyrite cement initially grew as framboids that diagenetically evolved into colloform, spherules, zoned and massive forms (Fig. 9C–F). It developed along the cleavage planes and fractures of the different rock-forming and heavy minerals (Fig. 9D). The paragenetic sequence of minerals indicates that pyrite cement postdates the diagenetic smectite and carbonate cements in the lower unit. The chemical composition of pyrite cement indicates that it is pure and consists of Fe (average. ~46.5%) and S (average. ~53%) (Appendix 3). The different forms of pyrite cement are partially to completely oxidized in the middle and upper units (Fig. 9G–I). Pentlandite occurs as cross-cutting, cavity- and fracture filling (Fig. 10A–C) or as replacing phases for monazite and quartz (Fig. 10D–I). The formation of Fe and Ni sulfide is associated with hydrothermal alteration of monazite to apatite and thorite and corrosion of quartz (Fig. 10G–I). X-ray elemental mapping showed that the Fe–Ni sulfides are zoned and the zoning is not obvious in SEM/BSE images. This mineral assemblage is dominated in the southern part of the study area and almost absent in the central and northern parts of the study area.

Other sulfide minerals such as chalcopyrite, gersdorffite, arsenopyrite and sphalerite are less common in the weathered diamictites of the study area and occur mainly as small irregular grains in rock clasts and rarely occur as free detrital grains in the diamictite matrix.

4.4.4. Monazite, xenotime and apatite

The REE phosphates (e.g., monazite, xenotime and apatite) and zircon are more common in diamictite in the central and northern parts and locally in the southern part of the study area. Monazite grains rarely exceed 150 µm in size and sometimes contain inclusions of zircon. In the lower unit, monazite and xenotime have been altered to apatite and/or thorite along their margins, cleavage and internal fractures (Figs. 10G, H and 11A). Zircon occurs as euhedral zoned grains that are stable and unaltered in the lower unit. A few grains have been replaced by calcareous cement (Fig. 11B). Concentric zoning is observed in some monazite grains with rims typically higher in Th than cores. Elemental maps and BSE images showed that monazite grains are partially corroded, pitted, dissolved or replaced mainly by siliceous and argillaceous cements in the oxidation zone, (Fig. 11C–F). Dissolution of REE-bearing phosphate minerals and corrosion of quartz led to formation of colloform phosphorus-rich cerite and cavity-filling quartz (Fig. 11G–I).

5. Discussion

5.1. Glacial processes and mechanical dispersal

Late Paleozoic glaciated terrains (e.g., Australia) and Pleistocene (e.g., Canada, the northern USA, northern Europe and Asia, and alpine areas of South America) are a specific example of areas with transported cover. Understanding the stratigraphy, textures of the cover sediment and paleotopography of the underlying basement rocks are critical factors for mineral exploration and provenance assessment in areas of deep transported cover. The variation in thickness of the Permo-Carboniferous sedimentary sequence (28 m to 181 m) and its lateral discontinuous extension and changes into residual saprolite in the Agnew–Lawlers District suggest that the Permo-Carboniferous glacial sediments were deposited in small scattered, asymmetrical basins between paleohighs (Fig. 12A, B). Stratigraphic and facies analyses indicated that the diamictites consist of polymictic, very poorly sorted and matrix-supported clasts suggesting subglacial denudation of bedrock

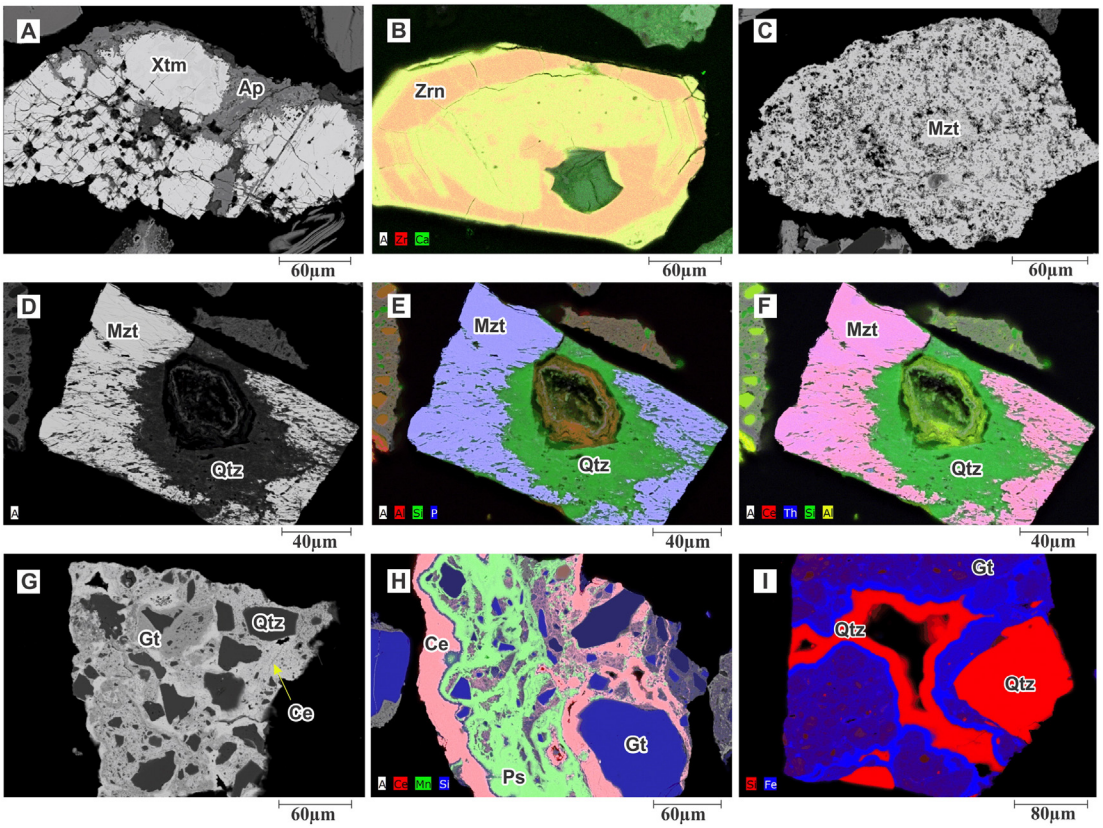

Fig. 11. Petrographic examination of non-opaque heavy minerals. A) A BSE image showing a xenotime grain replaced by apatite (Ap). B) An X-ray element map showing the distribution Zr and Ca in zircon (Zrn). C) A BSE image showing a spongy texture of a pitted monazite grain. D–F) A BSE image (D) and X-ray element maps (E & F) showing a monazite grain replaced by microcrystalline quartz (Qtz) and the distribution of Ce, Th and P in monazite and Si in silica cement and Al in an unknown altered mineral inclusion. G) A BSE image showing corroded quartz grains (Qtz) floating in ferruginous cement and bright cerite (Ce) cement. H) An X-ray element map showing the distribution of Ce, Mn and Si in the manganiferous (Ps) and cerite (Ce) cements and quartz grains (Qtz). I) An X-ray element map showing the distribution of Si and Fe in the ferruginous cement (Gt) and cavity-filling colloform quartz (Qtz) cement. (For interpretation of the references to color in this figure legend, the reader is referred to the web version of this article.)

(paleohighs) and deposition of the eroded debris within short lateral distances from the source rocks. The short distance of glacial transport, and thus proximal source rocks is also indicated by the angularity of mafic, ultramafic and BIF clasts in the southern part of the study area, by the abundance of locally derived boulders in the diamictites, and by the preservation of the euhedral outlines of opaque heavy minerals (Figs. 7A and 9A). On the other hand, rounded to subrounded, striated and facetted clasts of granitoids and granitic gneisses cover the Scotty Creek mafic-dominated, metasediments in the central and northern parts of the study area (Fig. 12A, B). This probably indicates that these clasts are far-traveled and derived from distal source of granitoids and granitic gneisses in the northwest to the southeast of the study area and mixed locally with clasts derived from metavolcanics and metasediments. The difficulty of assessing clast orientation from drilling data and the very poor sorting and organization of clasts within diamictites argue against direct deposition from the ice base which gives rise to tills with preferred clast orientation associated with pavements (Eyles & de Broekert, 2001). Instead, poorly sorted diamictites at Agnew area were deposited when basal debris is deposited in situ by melting of ice followed by local transport possibly by mass flow down bedrock slopes (Eyles & de Broekert, 2001).

The fine-grained fluvio-glacial sandstones and the glaciolacustrine siltstones, claystones and fine sandstones were considered as second and third derivatives of bedrock (Shilts, 1993). The sand and gravel that comprise glaciofluvial deposits are primarily derived from debris carried by the glacier. Glaciolacustrine sediments generally comprise the fine-grained debris that is washed from the glacier's load by glaciofluvial processes and flushed through the glaciofluvial system. Subsequent to glacial and glaciofluvial transport, silt and clay can remain in suspension for some time because of their fine grain size, and they can be deposited away from their source owing to dispersal by currents in lakes (Shilts, 1993). The geochemistry and mineralogy of the fluvio-glacial and glaciolacustrine sediments tends to be homogeneous over large areas with enrichments in REE and HFSE. Thus, these sediments cannot be used as indictors of the bedrock sources (Shilts, 1993). These sediments can accumulate rapidly in quiet-water lakes immediately in front of the glacier and may not undergo more dispersal than the glaciofluvial sediments or tills from which they are derived (Fig. 12B). Fluvio-glacial and glaciolacustrine sediments generally are not considered as a useful sample medium for mineral exploration.

5.2. Post-glacial weathering and hydromorphic dispersion

Chemical weathering of Permo-Carboniferous glacial sediments and hydromorphic dispersion of elements are associated with climatic changes in the late Cretaceous-early Tertiary greenhouse conditions (Pillans, 2007) and significantly affects the geochemistry of glacial sediments (Fig. 12C). Apatite fission track thermochronology suggests rapid burial in the early Permian, followed by denudation of ~2.5 to 3 km from the early Permian to the mid Jurassic/early Cretaceous (Weber et al., 2005). At Agnew, weathering produces a color change from oxidized, bleached white and brown diamictites at shallow depths to reduced, gray, unweathered diamictites at greater depth. Such color changes are also observed in the recent till deposits in Canada (McClenaghan et al., 2000), but at much shallower depths (tens of centimeters). In this study, these color variations are associated with mineralogical and chemical changes that led to subdivision of the Permo-Carboniferous sedimentary

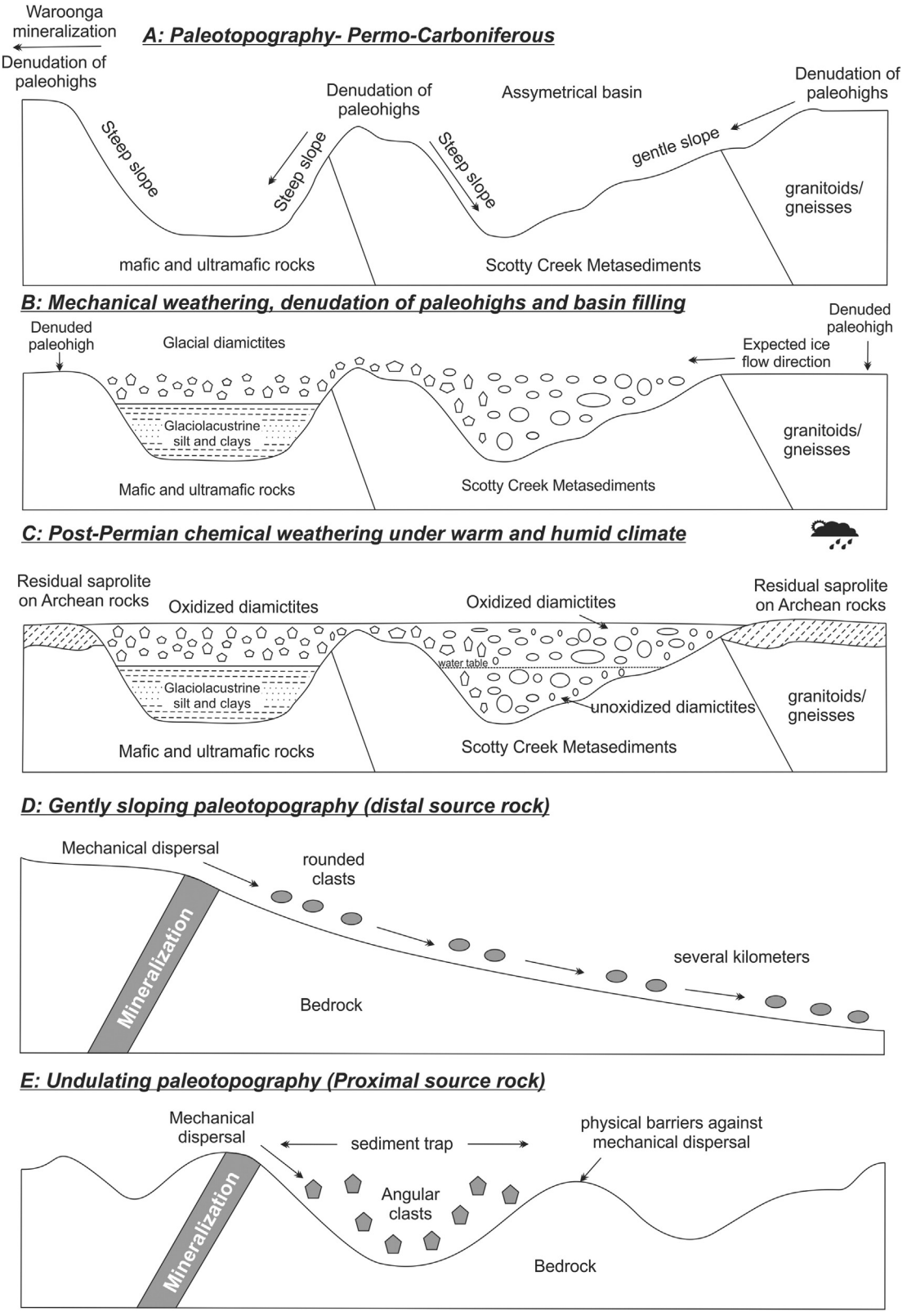

Fig. 12. Simplified model explaining the different stages of landscape evolution and paleoclimatic changes during the Permo-Carboniferous and post-Permian weathering. A) A proposed Permo-Carboniferous paleotopography. B) Denudation of paleohighs during glacial weathering of the bedrock and filling of basins by diamictites and glaciolacustrine sediments. C) Post-Permian chemical weathering and hydromorphic metal dispersion under warm and humid climate. D and E) Proposed sketches for distal mechanical dispersal along gently sloping paleotopography (E) and proximal mechanical dispersal along undulating paleotopography (F).

sequence into three main chemostratigraphic units. Oxidation–reduction, acid–base and hydrolysis processes across the redox boundary (interface 2, Figs. 3 and 13) are the main chemical changes affecting most of the rock-forming and accessory heavy minerals and causing element recycling. At some sites and the present study, Fe oxides have been derived from oxidized sulfides.

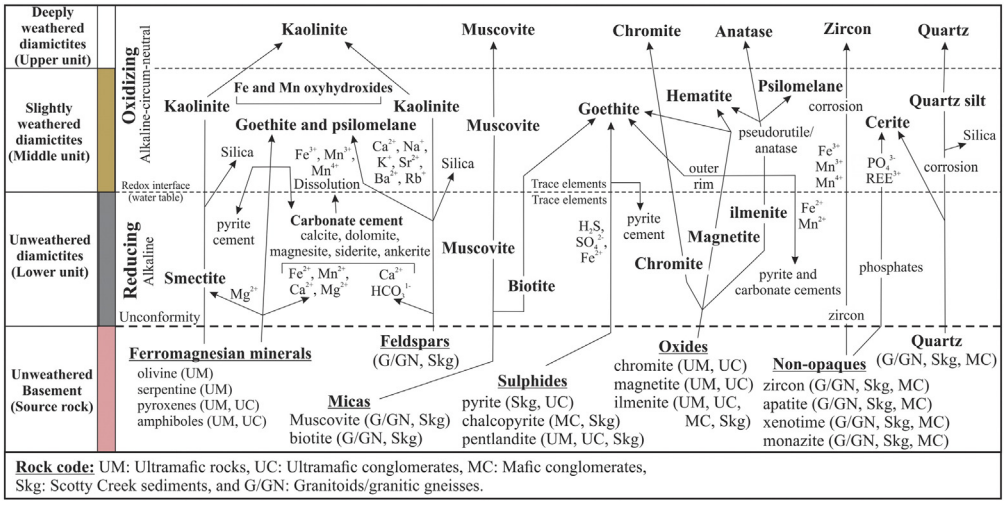

Fig. 13. Mineralogical alteration, metal release and recycling along the redox interface between the unweathered diamictites (lower chemostratigraphic unit) and weathered diamictites (middle and upper chemostratigraphic units) under Eh and pH gradients of reducing and alkaline condition in the lower unit to oxidizing and circum-neutral condition in the middle and upper units. (For interpretation of the references to color in this figure legend, the reader is referred to the web version of this article.)

Detrital sulfides such as pyrite, pyrrhotite, chalcopyrite and arsenopyrite are dominant in the Scotty Creek metasediments, whereas pentlandite is more common in the mafic–ultramafic rocks and conglomerates (Fisher et al., 2011). Sulfides are stable under anoxic conditions but are easily oxidized above the redox boundary (interface 2). They are chemically unstable and physically weak during the typical conditions of glacial transport and deposition. Their preservation as euhedral-subhedral grains in the lower unit of the Permo-Carboniferous sedimentary sequence reflect short distance of glacial transport from proximal sources and/or the dominance of reducing condition after deposition. Oxidative dissolution of detrital sulfides, together with ferromagnesian and opaque heavy minerals, release Fe^{2+}, Mn^{2+}, SO_4^{2-} and other redox-sensitive trace elements (e.g., As, Co, Cu, Mo, Ni and Zn) along redox fronts. Such paleoredox front (s) represent traps for metal enrichment during sedimentation, diagenesis or weathering and thus can be specifically targeted for sampling during exploration drilling because they are associated with organic matter and/or sulfide or Fe oxides (Shilts, 1993; Lawrance, 1999; Butt et al., 2008; Anand & Robertson, 2012). In Agnew district, redox-sensitive elements such as Cu, As, Ni, Co and V are reprecipitated with, or adsorbed on the surfaces of, Fe and Mn oxyhydroxides and oxides (e.g., goethite and psilomelane). The hydromorphic dispersion of As, Co, Cu, Mo, Ni and Zn is best detected in the fine fraction (typically <2 mm) of weakly oxidized diamictites (Cohen & Bowell, 2014). These elements are also recycled and reprecipitated as secondary framboidal pyrite and is diagenetically transformed into colloform and zoned pyrite below the redox boundary under euxinic condition (Fig. 9C–F). These textures probably reflect initial precipitation from supersaturated, colloidal solution with a rapid nucleation rate (Butler & Rickard, 2000). Pyrite cement is dominant in the central and northern parts of the study area where detrital sulfides are dominated in the Scotty Creek metasediments. The secondary oxidation of pyrite cement and the presence of few surviving sulfide grains in the oxidized zone reflects successive phases of oxidation-reduction due to oscillation of water table (Fig. 9G–I).

Progressive destruction of ferromagnesian minerals (serpentine, chlorite, olivine, pyroxenes, amphiboles and biotite) releases Ca^{2+}, Mg^{2+}, Fe^{2+} and Mn^{2+} that combined with HCO_3^-/CO_3^{2-} anions derived from hydrolysis of feldspars under alkaline conditions to form calcareous cement (calcite, magnesite, dolomite, siderite and ankerite). These carbonate minerals are easily dissolved under acidic conditions (Fig. 13). Hydrolysis of feldspars releases Ca^{2+}, Na^+, K^+, Sr^{2+}, Ba^{2+}, Rb^+ and Cs^+ that can then be incorporated in the structures of goethite and psilomelane, whereas Al and Si are retained in clays and silica. The rate of pyrite oxidation can be enhanced in the presence of carbonate under alkaline (pH < 10) conditions (Caldeira et al., 2010). This reaction generates acidity that was buffered by carbonates generation and maintained a favorable pH condition for the precipitation of iron hydroxides and sulfates (Descostes et al., 2002; Caldeira et al., 2010).

5.3. Indicator heavy mineral composition

In general, detrital heavy mineral assemblages are common constituents of most sediments. They undergo modifications during the different stages of the sedimentary cycle (Morton & Hallsworth, 1999; van Loon & Mange, 2007). Despite decades of intensive studies (e.g., Nickel, 1973; Pettijohn et al., 1987; Morton & Hallsworth, 1999; Milliken, 2007; Morton & Hallsworth, 2007), these modifications are still poorly understood. Sulfides, opaque oxide and non-opaque heavy minerals are the main carriers of ore-related trace elements (e.g., Cu, Co, Ni and Zn). Therefore, understanding heavy mineral transport and preservation mechanisms is important not only for provenance studies, but also for interpreting the geochemistry of sediments (e.g., Van Loon & Mange, 2007). Tracking indicator mineral grains dispersed in till and stream sediments is common exploration method for mineral deposits in recently glaciated terrains (e.g., McClenaghan et al., 2000; McClenaghan & Kjarsgaard, 2001; Kjarsgaard et al., 2004; Lehtonen et al., 2005).

Being affected by a climatic shift from icehouse in Permo-Carboniferous to greenhouse tropical condition in late Cretaceous–early Paleocene (Pillans, 2007), a Permo-Carboniferous glacial sedimentary sequence in the Agnew–Lawlers, gold-rich district is a particularly rewarding area for studying heavy mineral provenance and post-depositional, chemical weathering and dissolution.

Heavy minerals tend to weather less rapidly than other rock-forming minerals (e.g., Morton & Hallsworth, 2007), however, it is possible to follow the weathering and diagenetic pathways of the opaques that are readily altered through changing oxidizing and reducing geochemical environments (Weibel & Friis, 2007). Textural, mineralogical and chemical modifications might occur in these minerals while exposed to an acidic, temperate to subtropical–tropical climatic weathering (Van Loon & Mange, 2007) and/or diagenetic alteration that potentially can complicate provenance studies (Morton, 1984; Milliken, 1988; Schroeder et al., 2002). It is therefore critical that the parameters used for interpretation of provenance reflect source area characteristics, rather than subsequent weathering or diagenetic processes (Morton & Hallsworth, 2007). In the oxidizing environment, ilmenite initially altered through leaching and

oxidation of Fe^{2+} and Mn^{2+} during weathering and produced pseudorutile (a mineral with a well-defined structure) which breaks down upon further alteration to leucoxene (Mücke & Chaudhuri, 1991) and finally to either rutile or anatase (Anand & Gilkes, 1984; Pe-Piper et al., 2005). The Fe that is released by this process is available to form such neomorphic or diagenetic minerals as goethite, hematite, pyrite, siderite and chlorite. This process can be represented by the two model reactions. The first is the anodic oxidation to pseudorutile through a solid-state transformation in which Fe^{2+} and Mn^{2+} are oxidized and removed from the rhombohedral structure to produce an intermediate pseudorutile phase (Grey & Reid, 1975). The second is an incongruent dissolution of pseudorutile and precipitation of anatase, rutile, hematite, and Mn oxide. Pseudorutile can form as an intermediate phase from ilmenite during weathering (Anand & Gilkes, 1984; Schroeder et al., 2002, 2004), or diagenesis (Pe-Piper et al., 2005). Complete weathering of ilmenite would lead to a TiO_2 polymorph through pseudorutile/leucoxene as reflected by the Ti/(Ti + Fe) ratios (ilmenite (<0.50) ⇒ pseudorutile/leucoxene (0.50 to 0.95) ⇒ rutile/anatase (>95)) (Pe-Piper et al., 2005). The elemental maps and variations of MnO with Ti/(Ti + Fe) suggest that Mn was almost completely leached during the gradual alteration of ilmenite to rutile or anatase.

In the reducing environment, ilmenite grains are slightly altered to leucoxene (generally > 70% TiO_2) and the exsolved Mn-rich hematite lamellae are dissolved. This process results in liberation of Fe^{2+} and Mn^{2+} that could participate in the precipitation of framboidal pyrite (Morad & AlDahan, 1986; Weibel & Friis, 2007) and siderite and ankerite cements within the pseudomorphs or in the adjacent pore space.

Ilmenite is almost recorded in all basement (source) rocks including ultramafic–mafic rock association, mafic and ultramafic conglomerates and Scotty Creek metasediments (Fisher et al., 2011). Ilmenite was subjected to hydrothermal alteration to titanite in the source rocks for example at Crusader gold deposit (Jowitt et al., 2014). This type of alteration is recoded mainly in ilmenite from the Scotty Creek metasediments and not recorded in ilmenite from mafic and ultramafic rocks and conglomerates at the Waroonga deposits (Fisher et al., 2011). Ilmenite altered to titanite is preserved in the lower unweathered diamictite unit and this complicates tracing the weathering history of ilmenite and indicates that not all of the Ti-oxides in the pseudomorphs are a product of weathering. Ilmenite in the source rocks varies in its Mn content from 0.32 to 5.42 wt.% and is Mn-rich (>3% MnO) in the Waroonga deposits (Fisher et al., 2011). It has been suggested that Mn-rich ilmenite (>4% MnO) is abundant in some peraluminous granite and metapelites, whereas low-Mn ilmenite is known to occur in both mafic igneous and metamorphic rocks in the source area (Pe-Piper et al., 2005). It has been also noted that in general ilmenite from metamorphic rocks is richer in TiO_2 than ilmenite in igneous rocks (Basu & Molinaroli, 1991; Schneiderman, 1995). Conversely, Schroeder et al. (2002) carried out a detailed investigation of the phases of ilmenite weathering in weathering profiles on granite and ultramafic rocks in the Georgia Piedmont, eastern USA and they concluded that ilmenite grains from the granite profile are more rich in Mn than those from the schist profile that contain minor amounts of Mn. In the present study, the co-existence of altered ilmenite together with quartz, apatite, albite and chlorite in the same detrital rock clasts, as well as the presence of abundant inclusions of zircon and apatite in ilmenite, may indicate that ilmenite is derived from felsic source rocks. Fisher et al. (2011) described similar mineralogical association in the metasedimentary Scotty Creek sandstones.

Chrome-spinel minerals are considered to be an exceptionally chemically stable and durable detrital mineral (Butt et al., 2000; Morton & Hallsworth, 2007; Mange & Morton, 2007). Recent studies showed that chromite can alter during weathering and pedogenic (soil) processes (e.g., Garnier et al., 2008). In the present study, zoned chromite is stable under reducing environment, whereas in the oxidation zone, the inner chromite core is stable, while the outer Cr-magnetite rim and magnetite of the banded iron formation are altered into hematite and goethite. The Cr-magnetite grains are partially or completely altered along the internal cracks into goethite that is enriched in SiO_2, Al_2O_3, ZnO and V_2O_3 relative to Cr-magnetite rim. Magnetite is stable under alkaline and reducing conditions, but dissolved under acid to neutral conditions with the exception of rare cases where they were protected by early cement (e.g., clays) (Weibel & Friis, 2007). Magnetite is partially to completely replaced by hematite (martite) under the oxidizing conditions. The mechanism of martitization (hematization of magnetite) could involve an intermediate phase of maghemite (γ-Fe_2O_3), or a compound intermediate in composition between Fe_3O_4 and Fe_2O_3 or the direct formation of hematite (α-Fe_2O_3) from magnetite (Fe_3O_4) (Turner, 1980). Hematite with martite texture is thus a characteristic alteration product of magnetite forming under oxidizing diagenetic conditions (Weibel & Friis, 2007). The increase in abundance of chromite, Cr-magnetite and magnetite in the southern part, and locally in the northern part of the study area, is explained by the proximal mafic–ultramafic source rocks. Fisher et al. (2011) identified chromite, Cr-magnetite and magnetite in ultramafic rocks and ultramafic conglomerates in Waroonga deposits. These minerals are not recorded in the mafic conglomerates and the Scotty Creek metasediments (Fisher et al., 2011).

Phosphates like monazite, xenotime, and apatite, together with zircon, are known to be exceptionally stable detrital heavy minerals during the sedimentary cycle of siliciclastic sediments (Pettijohn, 1975). The stability of these minerals in the lower unweathered unit provides information about the source rock geology. These non-opaque heavy minerals are associated with ilmenite, quartz, sodic plagioclase, biotite and hornblende in the diamictite the central and northern parts of the study area. This mineral assemblage is probably derived from felsic source rock. Monazite is closely associated with or replaced by Ni, Co, Cu and Fe sulfides (pentlandite, pyrite and chalcopyrite) in the southern part of the study area where the diamictite is close to mafic–ultramafic source rocks. Element mapping showed that pentlandite also occurs as cavity- and fracture-filling zoned grains with increase in Ni and Co toward external zones. The alteration of monazite to apatite and thorite/huttonite as well as its replacement by pentlandite may provide evidence of felsic intrusive-related hydrothermal alteration of the source rocks. The hydrothermal alteration of monazite and the subsequent precipitation of Ni sulfides can present an opportunity for further possible exploration of proximal base metal mineralized target in the gold-rich region. The hydrothermal alteration was suggested by Jowitt et al. (2014) for the Crusader ore bodies, where the gold is generally intimately associated with magnetite and is characterized by elevated concentrations of Mo, Be, Li, Sn and Fe, and depletions in Na, Cu, Ba, Pb, Mn, Zn, Si, and K. The altered monazite co-exists with pristine monazite grains that show no sign of alteration in the source rocks, indicating that the alteration did not take place in situ in the sediments. In general, monazite, apatite, zircon and possibly xenotime are unstable during chemical weathering under tropical climatic conditions (Morton, 1986). They are readily etched, pitted, dissolved and replaced by silica and ferruginous cements in the oxidation zone (middle and upper units). Experimental studies of accessory phosphate mineral solubility in aqueous fluids suggest that monazite and apatite solubility in pure H_2O is low, and increases with decreasing pH (Nickel, 1973; Ayers & Watson, 1991). Acidic conditions created above the redox interface were maintained by the oxidation of sulfides that enhanced dissolution of the phosphate minerals and corrosion and fragmentation of quartz (Salama, 2014). These processes led to leaching of LREE and P from phosphate and Si from quartz and aluminosilicates to form colloform and cavity-filling cerite cement. The precipitation of cerite cement could be related to the buffering effect of carbonate for the sulfide oxidation.

5.4. Provenance and sampling media for mineral exploration

The heavy mineral separates were used in this study as indicators to assess the source rocks of the Permo-Carboniferous sedimentary

sequence in the Agnew area. Weathering of near-surface diamictites restricts the use of heavy minerals in prospecting for economic minerals, with the exception of resistate ore minerals or their indicators (e.g., chromite). However, the preservation of unweathered diamictites at the base of the Permo-Carboniferous glacial succession at Agnew area provides an opportunity for using these sediments to target mineralization. Mafic and ultramafic clasts in diamictite, together with their component sulfides (e.g., pentlandite) and oxides (e.g., magnetite, chromite and low-Mn ilmenite), are relatively abundant in the southern part and locally in the central part of the study area close to the mafic and ultramafic rocks (e.g., drill hole EMSC4738). These minerals are typically hosted in ultramafic rocks and are only observed in parts of the ultramafic conglomerates at the Waroonga deposits (Fisher et al., 2011). Zoned chromites show strong Cr-rich core-Fe-rich rim zonation with chromite cores and magnetite rims is hosted mainly in the komatiitic serpentinites in Agnew area (Fisher et al., 2011). The presence of few chromite grains without zoning (Fig. 7A) may indicate different unmetamorphosed or weakly metamorphosed source rocks such as the ultramafic conglomerates. Magnetite, chromite, low-Mn ilmenite and pentlandite decrease in abundance toward the central and northern parts of the study area where the Permo-Carboniferous sequence is underlain and surrounded by Scotty Creek metasediments and granitoids. The Scotty Creek metasediments consist of polymictic, volcanic conglomerates and sandstones dominated by mafic clasts with lesser felsic (granitic and dacitic) clasts (Squire et al., 2010). In contrast, diamictite clasts of granite, gneiss, metavolcanics, sulfide-bearing quartzite, metasediments and metavolcanics are dominant in the central and northern parts of the study area. The presence of rounded felsic diamictite clasts of granitoids/granitic gneisses above the mafic-dominated metasediments in the central part and the mafic–ultramafic rocks in the southern part and the presence of glaciolacustrine sediments at the southern part of the study may indicate that these clasts were transported from distal granitoids/granitic gneiss in the northwest of the study area to the southeast of the Lawlers Anticline (Fig. 1B). However, when plotted in ternary diagrams, chemical analysis of the unweathered diamictites of the lower chemostratigraphic unit is well correlated to the Scotty Creek metasediments (Fig. 5). This might suggest that the Scotty Creek metasediments are the main source rock of the Permo-Carboniferous sediments in the studied area. Zircon, apatite and monazite increase toward the central and northern parts of the study area. These heavy minerals may reveal felsic source rocks. Ilmenite is the most abundant and widely distributed heavy and its presence indicates the dominance of mafic source rocks. Pyrite also increases as detrital and secondary framboidal and colloform cementing phases at the expense of oxide minerals in the central and northern parts. This cement is most probably derived from the dissolution of pre-existing detrital primary sulfides.

Gold mineralization in the Agnew–Lawlers area is located along the western limb of the Lawlers anticline in a linear N–S striking Emu shear zone (Jowitt et al., 2014). These gold deposits include Waroonga, Redeemer, Crusader/Deliver and Songvang. The gold mineralization at Crusader is mainly associated with magnetite and locally with titanite and hosted in mafic and ultramafic rocks and mafic conglomerates (Jowitt et al., 2014). Therefore, ilmenite, chromite, magnetite and primary detrital sulfides are the significant heavy minerals that should be searched for in the diamictite. These minerals are most abundant in the Permo-Carboniferous sediments of the southern part (~2.25 km^2), which directly overlie and are surrounded by the mafic–ultramafic rocks. Although the Permo-Carboniferous sediment sequence is ~1.5 km NE of the Waroonga gold Pit, ~1 km in length and <100 m in width (Fisher et al., 2011), gold grains have not recorded in the diamictite matrix and clasts or in the heavy mineral concentrates. Gold content in the Permo-Carboniferous diamictites and rhythmites is generally low (up to 29 ppb) in the Agnew area. This may indicate that the source rocks of the Permo-Carboniferous sediments are generally barren or gold-poor. Therefore gold itself is not a useful geochemical indicator of the presence of gold mineralization in the source rocks. In addition, the proposed ice flow direction and mechanical dispersal of Permo-Carboniferous glacial sediments to the southeast toward the Waroonga gold deposits explains the low content or absence of gold in these sediments. Therefore, there is no link between the Waroonga gold deposits and Permo-Carboniferous glacial sediments. Lateral variations in thickness, irregular basement paleotopography and asymmetry of the depositional basins indicate that mechanical dispersal of the Permo-Carboniferous glacial sediments was locally affected by paleotopographic highs that probably acted as physical barriers against transportation from the source rocks (Fig. 12A and E). This suggests that the current distribution of Permo-Carboniferous sediments across the Yilgarn Craton may be restricted to isolated basins between paleohighs rather than larger paleochannels. Therefore, mineral exploration through the Permo-Carboniferous sedimentary cover in the Yilgarn Craton is likely to give a clue to a mixed proximal and distal source rocks (Fig. 12A and D). However, the wide-spaced drilling and the discontinuous lateral distribution of the Permo-Carboniferous sediments in the study area are limitations in characterizing the style of glacial transport in Agnew area. Mixing of angular and rounded clasts derived from proximal and distal source rocks and the presence of fluvioglacio- and glacio-lacustrine sediments may provide evidence of a continental glaciation style.

A sampling strategy for the Permo-Carboniferous glacial sediments in the Yilgarn Craton should involve targeting the Permo-Carboniferous/basement nonconformity (interface 1). This physical interface is marked by a boulder bed, where rock-forming and opaque (e.g., sulfide and oxide) indicator heavy minerals are still preserved and can be used potentially to determine the source rocks for the sediments and mineralization. Sampling basal conglomerates at this interface are effective for mineral exploration in other depositional regimes (Butt et al., 2008; Anand & Butt, 2010; Anand & Robertson, 2012).

The second important sampling medium is the redox interface separating reduced and oxidized sediments of lower and middle Permo-Carboniferous units. The interface reflects the post-depositional history and hydromorphic metal dispersion that depends mainly on the locally derived sediments from proximal source rocks. In this environment, hydromorphic dispersions of metals occurred by developing a redox gradient between the water table between the reduced sulfide-rich sediments and the overlying oxidized sediments. This resulted in a slight decrease of the pH in the Permo-Carboniferous sediments which enhanced the mobility of trace elements such as Ni, As, Cu and Zn and rare earth elements. These elements are better stored in the ferruginous and manganiferous cements and fine fractions of the matrix. The variation in cement type in the lower unweathered unit from calcareous in the southern part to pyrite in the central and northern parts of the study area may give a clue about the bedrock composition or the composition of the lower unweathered unit. The dominance of calcareous cement in the southern part reflects the mafic–ultramafic bedrocks. The dominance of pyrite cement in the central and northern parts reflect a proximal sulfide source or sulfide-rich sediments, even if sulfides are not persistent and dissolved.

6. Conclusions

Integration of litho- and chemostratigraphy, sediment textures, rock-forming and heavy minerals, geochemistry and paleotopography of the depositional basin are critical factors for understanding mineral exploration and provenance assessment in areas of deep transported cover. Permo-Carboniferous glacial sediments at Agnew area are divided mainly into three main lithofacies; diamictites, glaciolacustrine rhythmites and glaciofluvial sandstones. Diamictites consist of matrix-supported, angular to subangular and very poorly sorted polymictic clasts set in matrix of sands, silt and clays. Mafic, ultramafic and BIF clasts of diamictites are dominant in the southern part of the study area and indicate proximal mafic and ultramafic source rocks. This is

supported by the abundance of euhedral chromite, Cr-magnetite, magnetite and pentlandite. On the other hand, diamictite in the central and northern parts of the study area consists mainly of rounded granitoids/granitic gneisses that mixed with locally derived clasts of metavolcanics and metasediments. These clasts derived from the granitoids/granitic gneisses in the west of the study area and transported southeast and covering the Scotty Creek metasediments. This is supported by the abundance of monazite, apatite, zircon and less frequent xenotime in the central and northern parts of the study area. Altered monazite grains are also observed in the southern part with fracture-filling Ni sulfides that may indicate the presence of unexposed, felsic intrusive-related hydrothermal mineralization. Ilmenite is distributed in the different parts of the study area, but its chemistry can be used to differentiate between mafic (MnO > 4 wt.%) and felsic (MnO < 4 wt.%) source rocks. Opaque sulfides (primarily pyrite) were identified in unweathered diamictite in the central part as detrital grains and secondary cement.

Chemical analyses of the Permo-Carboniferous sediments indicate that they can be subdivided into three chemostratigraphic units based on degree of chemical weathering; 1) the lower unit is unweathered and composed of gray, calcareous diamictites and/or rhythmites that is characterized by high concentrations of Cr, Ni, Ca, Mg and S; 2) the middle unit is composed of slightly weathered, ferruginous diamictites and/or rhythmites that is characterized by high concentrations Fe, Mn, and transition elements; and 3) upper unit is composed of intensely weathered, kaolinitic diamictites that is characterized by high concentrations Al, Si and HFSE.

Diamictites of the lower chemostratigraphic unit are the optimal sampling medium that can be directly applied to assess different provenances because they still contain unweathered sulfide and oxide heavy minerals. In contrast, glaciofluvial and glaciolacustrine sediments, which were formed during melting of ice, dispersed far from the source rocks in front of the glacier. Thus, these sediments are not regarded as a useful sample medium. Interface sampling along the redox boundary (interface 2) is also important because it reflects the hydromorphic dispersion and metal recycling that is associated with paleoredox fronts and groundwater oscillation.

Supplementary data to this article can be found online at http://dx.doi.org/10.1016/j.oregeorev.2015.07.014.

Conflict of interest

No conflict of interest.

Acknowledgment

The work has been supported by the Deep Exploration Technologies Cooperative Research Centre (DET CRC) whose activities are funded by the Australian Government's Cooperative Research Centre Programme. This is DET CRC document 2015/662 and approved for publication. We wish also to thank management and staff of Gold Fields Ltd., for their cooperation and hospitality, without which these studies would have been difficult. Special thanks for Ian Pegg and Takeshi Uemoto for providing RC chip trays, maps and drilling data. We gratefully acknowledge Angelo Vartesi for the drafting of Fig. 1A. Ray Smith and Mel Lintern from CSIRO and two anonymous reviewers are thanked for providing critical reviews of the manuscript.

References

Anand, R.R., 2005. Weathering history, landscape evolution and implications for exploration. In: Anand, R.R., De Broekert, P. (Eds.), CRC LEME Monograph, CSIRO, Perth, pp. 2–40.

Anand, R.R., Butt, C.R.M., 2010. A guide for mineral exploration through the regolith in the Yilgarn Craton, Western Australia. Aust. J. Earth Sci. 57 (8), 1015–1114.

Anand, R.R., Gilkes, R.G., 1984. Weathering of ilmenite in a lateritic pallid zone. Clay Clay Miner. 32, 363–374.

Anand, R.R., Paine, M., 2002. Regolith geology of the Yilgarn Craton, Western Australia: implications for exploration. Aust. J. Earth Sci. 49, 3–162.

Anand, R.R., Robertson, I.D.M., 2012. The role of mineralogy and geochemistry in forming anomalies on interfaces and in areas of deep basin cover: implications for exploration. Geochem. Explor. Environ. Anal. 12, 45–66.

Anand, R.R., Fraser, S.F., Jones, M.R., Shu, Li, Munday, T.J., Phang, C., Robertson, I.D.M., Scott, K.M., Vasconcelos, P., Wildman, J.E., Wilford, J., 1997. Geochemical exploration in regolith-dominated terrain, north Queensland. CSIRO Australia, Division of Exploration and Mining Restricted Report 63R/E&M Report 447R (reissued as Open File Report 120, CRCLEME, Perth) (130 pp.).

Averill, S.A., 2001. The application of heavy indicator mineralogy in mineral exploration, with emphasis on base metal indicators in glaciated metamorphic and plutonic terrain. In: McClenaghan, M.B., Bobrowsky, P.T., Hall, G.E.M., Cook, S.J. (Eds.), Drift Exploration in Glaciated Terrains. Geol. Soc. Spec. Publ., London 185, pp. 69–82.

Averill, S.A., 2011. Viable indicator minerals in surficial sediments for two major base metal deposit types: Ni–Cu-PGE and porphyry Cu. Geochem. Explor. Environ. Anal. 11, 279–292.

Ayers, J.C., Watson, E.B., 1991. Solubility of apatite, monazite, zircon, and rutile in supercritical aqueous fluids with implications for subduction zone geochemistry. Philos. Trans. R. Soc. Lond. A 335, 365–375.

Basu, A., Molinaroli, E., 1991. Reliability and application of detrital opaque Fe–Ti oxide minerals in provenance determination. In: Morton, A.C., Todd, S.P., Haughton, P.D.W. (Eds.), Developments in Sedimentary Provenance Studies. Spec. Publ., Geol. Soc., London 57, pp. 55–65.

Blewett, R.S., Czarnote, K., Henson, P.A., 2010. Structural-event framework for the eastern Yilgarn Craton, Western Australia, and its implications for orogenic gold. Precambrian Res. 183, 203–229.

Bourman, R.B., Alley, N.F., 1999. Permian glaciated bedrock surfaces and associated sediments on Kangaroo Island, South Australia: implications for local Gondwanan ice-mass dynamics. Aust. J. Earth Sci. 46 (4), 523–531.

Broome, J., Journeaux, T., Simpson, C., Dodunski, N., Hosken, J., DeVitry, C., Pilapil, L., 1998. Agnew–Lawlers gold deposits. In: Berkman, D.A., Mackenzie, D.H. (Eds.), Geology of Australian and Papua New Guinean Mineral DepositsAusIMM Monograph 22. AusIMM the mineral institute, Melbourne, pp. 161–166.

Butler, I.B., Rickard, D., 2000. Framboidal pyrite formation via the oxidation of iron (II) monosulfide by hydrogen sulphide. Geochim. Cosmochim. Acta 64 (15), 2665–2672.

Butt, C.R.M., Lintern, M.J., Anand, R.R., 2000. Evolution of regolith and landscapes in deeply weathered terrain: implications for geochemical exploration. Ore Geol. Rev. 16, 167–183.

Butt, C.R.M., Robertson, I.D.M., Scott, K.M., Cornelius, M., 2005. Regolith Expressions of Australian Ore Deposits. CRC LEME, Optima Press, Perth.

Butt, C.R.M., Scott, K.M., Cornelius, M., Robertson, I.D.M., 2008. Regolith sampling for geochemical exploration. In: Scott, K.M., Pain, C.F. (Eds.), Regolith Science. CSIRO publishing, pp. 341–376.

Caldeira, C.L., Ciminelli, V.S.T., Osseo-Asare, K., 2010. The role of carbonate ions in pyrite oxidation in aqueous systems. Geochim. Cosmochim. Acta 74 (15) (1777–17).

Cameron, E.M., Hamilton, S.M., Leybourne, M.I., Hall, G.E.M., McClenaghan, M.B., 2004. Finding deeply buried deposits using geochemistry. Geochem. Explor. Environ. Anal. 4, 7–32.

Cassidy, K.F., Hagemann, S.G., 2001. 'World-class' Archean orogenic gold deposits, eastern Yilgarn Craton: diversity in timing, structural controls and mineralization styles. AGSO-Geoscience Australia Record 2001/37, Canberrapp. 382–384.

Champion, D.C., Sheraton, J.W., 1997. Archaean granitoids of the northern Eastern Goldfields Province, Yilgarn Craton, Australia: constraints on crustal growth. Precambrian Res. 83, 109–132.

Cohen, D.R., Bowell, R.J., 2014. Exploration geochemistry. In: Heinrich, H., Turekian, K. (Eds.), Geochemistry of mineral deposits, 2nd ed. Treatise on Geochemistry 13, pp. 623–649.

Crowell, J.C., Frakes, L.A., 1971. Late Palaeozoic glaciation of Australia. J. Geol. Soc. Aust. 17, 115–155.

Descostes, M., Beaucaire, C., Mercier, F., Savoye, S., Sow, J., Zuddas, P., 2002. Effect of carbonate ions on pyrite (FeS_2) dissolution. Bull. Soc. Geol. Fr. 173, 265–270.

Eppinger, R.G., Fey, D.L., Giles, S.A., Grunsky, E.C., Kelley, K.D., Minsley, B.J., Munk, L., Smith, S.M., 2013. Summary of exploration geochemical and mineralogical studies at the giant pebble porphyry Cu–Au–Mo deposit, Alaska: implications for exploration under cover. Econ. Geol. 108, 495–527.

Eyles, S.N., De Broekert, P., 2001. Glacial tunnel valleys in the Eastern Goldfields of Western Australia cut below the Late Palaeozoic Pilbara ice sheet. Palaeogeogr. Palaeoclimatol. Palaeoecol. 171, 29–40.

Eyles, N., Mory, A.J., Backhouse, J., 2002. Carboniferous-Permian palynostratigraphy of west Australian marine rift basins: resolving tectonic and eustatic controls during Gondwanan glaciations. Palaeogeogr. Palaeoclimatol. Palaeoecol. 184, 305–319.

Fisher, L.A., Sonntag, I., Barnes, S.J., Cleverley, L., Hough, R.M., 2011. Integrated 3D geochemistry and ore characterisation at the Agnew Gold Mine. Unpublished internal CSIRO technical report, Perth, pp. 162

Fletcher, I.R., Dunphy, J.M., Cassidy, K.F., Champion, D.C., 2001. Compilation of SHRIMP U–Pb geochronology data, Yilgarn Craton, Western Australia, 2000-01. Geoscience Australia, Canberra (Record 2001/047).

Foden, J.D., Nesbitt, R.W., Rutland, R.W.R., 1984. The geochemistry and crustal origin of the Archaean acid intrusives of the Agnew–Lawlers Dome, Lawlers, Western Australia. Precambrian Res. 23, 247–271.

Garnier, J., Quantin, C., Guimarães, E., Becquer, T., 2008. Can chromite weathering be a source of Cr in soils? Mineral. Mag. 72 (1), 49–53.

Grey, I.E., Reid, A.F., 1975. The structure of pseudorutile and its role in the alteration of ilmenite. Am. Mineral. 60, 898–906.

Hirvas, H., 1989. Application of glacial geological studies in prospecting in Finland. Drift Prospecting, Geological Survey of Canada, Paper 98-20, pp. 1–6.
Jowitt, S.M., Cooper, K., Squire, R.J., Thébaud, N., Fisher, L.A., Cas, R.A.F., Pegg, I., 2014. Geology, mineralogy, and geochemistry of magnetite-associated Au mineralization of the ultramafic–basalt greenstone hosted Crusader Complex, Agnew–Lawlers Gold Camp, Eastern Yilgarn Craton, Western Australia; a Late Archean intrusion-related Au deposit? Ore Geol. Rev. 56, 53–72.
Kelley, D.L., Hall, G.E.M., Closs, L.G., Hamilton, I.C., McEwen, R.M., 2003. The use of partial extraction geochemistry for copper exploration in northern Chile. Geochem. Explor. Environ. Anal. 3, 85–104.
Kjarsgaard, I.M., McClenaghan, M.B., Kjarsgaard, B.A., Heaman, L.M., 2004. Indicator mineralogy of kimberlite boulders from eskers in the Kirkland Lake and Lake Timiskaming areas, Ontario, Canada. Lithos 77, 705–731.
Klassen, R.A., 1997. Glacial history and ice flow dynamics applied to drift prospecting and geochemical exploration. In: Gubins, A.G. (Ed.), Proceedings of Exploration 97: Fourth Decennial International Conference on Mineral Exploration, pp. 221–232.
Krapež, B., Barley, M.E., Brosn, S.J.A., 2008. Late Archaean synorogenic basins of the Eastern Goldfields superterrane, Yilgarn Craton. Western Australia: part I. Kalgoorlie and Gindalbie Terranes. Precambrian Res. 161, 135–153.
Lawrance, L.M., 1999. Multi-element dispersion in Mesozoic basin sediment over the Osborne deposit, northern Queensland, Australia: implications for regional geochemical exploration in buried terrain. Exploration under cover. Aust. Ins. Geosci. Bull. 28, 73–81.
Lehtonen, M.L., Marmo, J.S., Nissinen, A.J., Johanson, B.S., Pakkanen, L.K., 2005. Glacial dispersal studies using indicator minerals and till geochemistry around two eastern Finland kimberlites. J. Geochem. Explor. 87, 19–43.
Levson, V.M., 2001. Regional till geochemical surveys in the Canadian Cordillera: sample media, methods and anomaly evaluation. In: McClenaghan, M.B., Bobrowsky, P.T., Hall, G.E.M., Cook, S.J. (Eds.), Drift Exploration in Glaciated Terrains. Geol. Soc. Spec. Publ., London 185, pp. 45–68.
Liu, S.F., Champion, D.C., Cassidy, K.F., 2002. Geology of the Sir Samuel 1:250 000 sheet area, Western Australia: Geoscience Australia, Record 2002/14, 57 pp.
Mange, M.A., Morton, A.C., 2007. Geochemistry of heavy minerals. In: Mange, M.A., Wright, D.T. (Eds.), Heavy Minerals in Use. Developments in Sedimentology 58, pp. 345–391.
Mange, M.A., Wright, D.T. (Eds.), 2007. Heavy Minerals in UseDevelopments in Sedimentology 58. Elsevier, Amsterdam (1283 pp.).
Mann, A.W., Birrell, R.D., Mann, A.T., Humphreys, D.B., Perdrix, J.L., 1998. Application of the mobile metal ion technique in geochemical exploration. J. Geochem. Explor. 61, 87–102.
McClenaghan, M.B., 2005. Indicator mineral methods in mineral exploration. Geochem. Explor. Environ. Anal. 5, 233–245.
McClenaghan, M.B., Kjarsgaard, B.A., 2001. Indicator mineral and geochemical methods for diamond exploration in glaciated terrain in Canada. In: McClenaghan, M.B., Bobrowsky, P.T., Hall, G.E.M., Cook, S.J. (Eds.), Drift Exploration in Glaciated Terrains. Geol. Soc. Spec. Publ., London 185, pp. 83–123.
McClenaghan, M.B., Thorleifson, L.H., DiLabio, R.N.W., 2000. Till geochemical and indicator mineral methods in mineral exploration. Ore Geol. Rev. 16, 145–166.
McClenaghan, M.B., Plouffe, A., McMartin, I., Campbell, J.E., Spirito, W.A., Paulen, R.C., Garrett, R.G., Hall, G.E.M., 2013. Till sampling and geochemical analytical protocols of the Geological Survey of Canada. Geochem. Explor. Environ. Anal. 13, 285–301.
McMartin, I., McClenaghan, M.B., 2001. Till geochemistry and sampling techniques in glaciated shield terrain: a review. In: McClenaghan, M.B., Bobrowsky, P.T., Hall, G.E.M., Cook, S.J. (Eds.), Drift Exploration in Glaciated Terrains. Geol. Soc. Spec. Publ., London 185, pp. 19–43.
Milliken, K.L., 1988. Loss of provenance information through subsurface diagenesis in Plio-Pleistocene sandstones, northern Gulf of Mexico. J. Sediment. Petrol. 58, 992–1002.
Milliken, K.L., 2007. Provenance and diagenesis of heavy minerals, Cenozoic units of the northwestern Gulf of Mexico sedimentary basin. In: Mange, M.A., Wright, D.T. (Eds.), Heavy Minerals in Use. Developments in Sedimentology 58, pp. 247–261.
Morad, S., AlDahan, A.A., 1986. Alteration of detrital Fe–Ti oxides in sedimentary rocks. Geol. Soc. Am. Bull. 97, 567–578.
Morton, A.C., 1984. Stability of detrital heavy minerals in Tertiary sandstones of the North Sea Basin. Clay Miner. 19, 287–308.
Morton, A.C., 1986. Dissolution of apatite in North Sea Jurassic sandstones: implications for the generation of secondary porosity. Clay Miner. 21, 711–733.
Morton, A.C., Hallsworth, C.R., 1999. Processes controlling the composition of heavy mineral assemblages in sandstones. Sediment. Geol. 124, 3–29.
Morton, A.C., Hallsworth, C., 2007. Stability of detrital heavy minerals during burial diagenesis. In: Mange, M.A., Wright, D.T. (Eds.), Heavy Minerals in Use. Developments in Sedimentology 58, pp. 215–345.
Mücke, A., Chaudhuri, J.N.B., 1991. The continuous alteration of ilmenite through pseudorutile and leucoxene. Ore Geol. Rev. 6, 25–44.
Myers, J.S., 1997. Preface: Archaean geology of the Eastern Goldfields of Western Australia-regional overview. Precambrian Res. 83, 1–10.
Nickel, E., 1973. Experimental dissolution of light and heavy minerals in comparison with weathering and intrastratal solutions. Contrib. Sedimentol. 1, 1–68.
Pe-Piper, G., Piper, D.W., Dolansky, L., 2005. Alteration of ilmenite in the Cretaceous sandstones of Nova Scotia, southeastern Canada. Clay Clay Miner. 53 (5), 490–510.
Pettijohn, F.J., 1975. Sedimentary Rocks. 3rd ed. Harper and Row, New York.
Pettijohn, F.J., Potter, P.E., Siever, R., 1987. Sand and Sandstone. Springer-Verlag, New York (553 pp).
Pillans, B., 2007. Pre-Quaternary landscape inheritance in Australia. J. Quat. Sci. 22 (5), 439–447.
Platt, J.P., Allchurch, P.D., Rutland, R.W.R., 1978. Archaean tectonics in the Agnew–Lawlers supracrustal belt, Western Australia. Precambrian Res. 7, 3–30.
Rose, A.W., Hawkes, H.E., Webb, J.S., 1979. Geochemistry in Mineral Exploration. 2nd ed. Academic Press, London.
Salama, W., 2014. Paleoenvironmental significance of aluminum phosphate–sulfate minerals in the upper Cretaceous ooidal ironstones, E-NE Aswan area, southern Egypt. Int. J. Earth Sci. 103, 1621–1639.
Salama, W., González-Álvarez, I., Anand, R.R., 2015. Significance of weathering and regolith/landscape evolution for mineral exploration in the NE Albany-Fraser Orogen. Western Australia. Ore Geol. Rev. http://dx.doi.org/10.1016/j.oregeorev.2015.07.024.
Sarala, P., Peuraniemi, V., 2007. Exploration using till geochemistry and heavy minerals in the ribbed moraine area of southern Finnish Lapland. Geochem. Explor. Environ. Anal. 7, 195–205.
Sarala, P., Pulkkinen, E., Juhani Ojala, V., Peltoniemi-Taivalkoski, A., 2009. Gold exploration using till at Petäjälehto, northern Finland. Geochem. Explor. Environ. Anal. 9, 247–255.
Schneiderman, J.S., 1995. Detrital opaque oxides as provenance indicators in River Nile sediments. J. Sediment. Res. A65, 668–674.
Schroeder, P.A., LeGolvan, J.J., Roden, M.F., 2002. Weathering of ilmenite from granite and chlorite schist in the Georgia Piedmont. Am. Mineral. 87, 1616–1625.
Schroeder, P.A., Pruett, R.J., Melear, N.D., 2004. Crystal-chemical changes in an oxidative weathering front in a middle Georgia kaolin deposit. Clays Clay Miner. 52, 212–220.
Sevastjanova, I., Hall, R., Alderton, D., 2012. A detrital heavy mineral viewpoint on sediment provenance and tropical weathering in SE Asia. Sediment. Geol. 280, 179–194.
Shilts, W.W., 1984. Till geochemistry in Finland and Canada. J. Geochem. Explor. 21, 95–117.
Shilts, W.W., 1993. Geological Survey of Canada's contributions to understanding the composition of glacial sediments. Can. J. Earth Sci. 30, 333–353.
Smee, B.W., 1998. A new theory to explain the formation of soil geochemical responses over deeply covered gold mineralisation in arid environments. J. Geochem. Explor. 61, 149–172.
Squire, R.J., Allen, C.M., Cas, R.A.F., Campbell, I.H., Blewett, R.S., Nemchin, A.A., 2010. Two cycles of voluminous pyroclastic volcanism and sedimentation related to episodic granite emplacement during the late Archean: Eastern Yilgarn Craton, Western Australia. Precambrian Res. 183, 251–274.
Turner, P., 1980. Continental red beds. Developments in Sedimentology 29. Elsevier Scientific Publishing Company, Amsterdam (562 pp.).
Van Loon, A.J., Mange, M.A., 2007. 'In situ' dissolution of heavy minerals through extreme weathering, and the application of the surviving assemblages and their dissolution characteristics to correlation of Dutch and German silver sands. In: Mange, M.A., Wright, D.T. (Eds.), Heavy Minerals in Use. Developments in Sedimentology 58, pp. 189–213.
Veevers, J.J., 1990. Tectonic-climatic supercycle in the billion-year plate-tectonic eon: Permian Pangean icehouse alternates with Cretaceous dispersed-continents greenhouse. Sediment. Geol. 68, 1–16.
Veevers, J.J., Saeed, A., Belousova, E.A., Griffin, W.L., 2005. U–Pb ages and source composition by Hf-isotope and trace-element analysis of detrital zircons in Permian sandstone and modern sand from southwestern Australia and a review of the palaeogeographical and denudational history of the Yilgarn Craton. Earth Sci. Rev. 68, 245–279.
Wang, X., Xie, X., Cheng, Z., Liu, D., 1999. Delineation of regional geochemical anomalies penetrating through thick cover in concealed terrains—a case history from the Olympic Dam deposit, Australia. J. Geochem. Explor. 66, 85–97.
Weber, U.D., Kohn, T.B.P., Gleadow, A.J.W., Nelson, D.R., 2005. Low temperature Phanerozoic history of the Northern Yilgarn Craton, Western Australia. Tectonophysics 400, 127–151.
Weibel, R., Friis, H., 2007. Alteration of opaque heavy minerals as a reflection of the geochemical conditions in depositional and diagenetic environments. In: Mange, M.A., Wright, D.T. (Eds.), Heavy Minerals in Use. Developments in Sedimentology 58, pp. 277–303.
Wilde, S.A., Valley, J.W., Peck, W.H., Graham, C.M., 2001. Evidence from detrital zircons for the existence of continental crust and oceans on the Earth 4.4 Gyr ago. Nature 409, 175–178.
Williams, I.R., 1975. Eastern Goldfields province. Geology of Western Australia. Western Australia Geological Survey Memoir 2, pp. 33–55.